Journal of the Brazilian Society of Mechanical Sciences and Engineering (2024) 46:641
https://doi.org/10.1007/s40430-024-05211-3

TECHNICAL PAPER

Bi-directional higher-order shear deformable mixed finite element formulation including couple effects for stresses of functionally graded curved 3d beams

Umit N. Aribas[1]

Received: 9 May 2024 / Accepted: 1 October 2024 / Published online: 9 October 2024

Abstract

This paper presents a formulation based on higher-order shear deformation functions in both normal and binormal directions on the cross section to include the influence of in-plane shear stresses in the case of curved beams subjected to out-of-plane forces. Besides, another distinctive feature is the introduction of accuracy elements at the stress concentration zones to widen the range of St. Venant principle. Within this scope, a two-noded curved mixed finite element formulation with twenty-eight degree of freedoms (DOFs) in total is derived. The curved axial geometry is defined over the exact functions of the gradient of arch length and curvature. The volume fraction of functionally graded (FG) material constituents is based on the power-law distribution and the rule of mixture. The functional including the coupling effects is derived via the Hellinger Reissner formulation. The normal/shear stresses are determined over the curvatures on the section and stress equilibrium condition. Quite satisfactory converged results with respect to the solid finite elements are obtained via advantageous DOFs for the bi-directional higher-order shear deformable mixed finite elements which reduces the computational time and space. Besides, in order to increase the precision at the stress concentration zones, the length ratios of the mixed finite elements at these zones are related to the geometric features and material parameters. Finally, the influences of geometric features, material constituents and the power-law index on the stress distribution of FG spatial/planar curved beams are presented both via the bi-directional higher-order mixed finite elements and the solid finite elements.

Graphical abstract

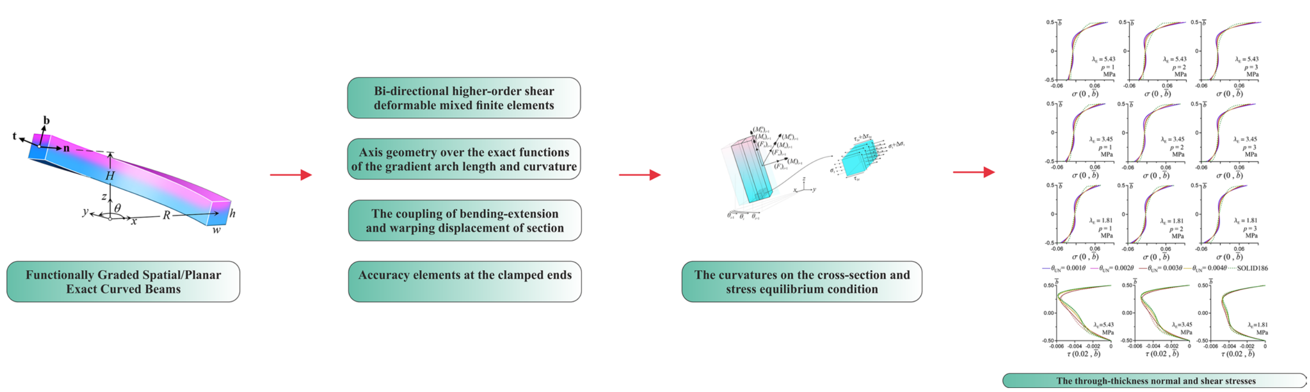

Keywords Higher-order shear deformation · Mixed finite element · Stress · Functionally graded · Curved beam

Technical Editor: Santosh Kapuria.

Extended author information available on the last page of the article

1 Introduction

1.1 Review

FG materials have been used in broad application fields over the last decades such as biological, aeronautical, naval, automotive, nuclear, military, civil engineering, etc., thanks to their physical performance. Therefore, their structural characteristics have aroused increasing interest of researchers [1–21]. Li et al. [22] proposed a novel higher-order shear deformable mixed beam element for stress distributions of functionally graded (FG) sandwich beams. Madenci [23] presented a mixed finite element (MFE) formulation for shear deformable FG thick–thin beams. Safa et al. [24] proposed a shear deformation theory including parabolic distribution of the transverse shear strains of FG beams. Lei et al. [25] derived a mechanical model based on a novel third-order shear deformation theory for bi-directional FG imperfect beams. Montalto and Konstantinidis [26] studied the buckling of higher-order shear deformable short beams subjected to the transverse shear. Bekhadda et al. [27] employed a four-variable refined higher-order shear deformable beam theory that considers the coupling of vibration and axial load of FG beams. Castañeda et al. [28] optimized higher-order shear deformation theories via the N-objective optimization evolutionary technique for the desired accuracy. Zhao [29] proposed an enhanced inverse finite element method based on the refined zigzag theory for composite beams. Malikan and Eremeyev [30] presented a novel hyperbolic-polynomial higher-order elasticity beam theory considering the stretching effect of thick FG imperfect beams. Melaibari et al. [31] employed the parabolic higher-order shear deformation theory for FG beams under variable axial load. Todorovska et al. [32] presented an analytical solution for the dynamic response of a shear beam. Li et al. [33] developed a 3-node beam finite element including higher-order shear deformations based on the arbitrary material distribution through thickness of FG beams. Pavan et al. [34] studied the static, free vibration and stability analyses of laminated composite beams via classical laminated plate, first-order shear deformation and higher-order shear deformation theories. Ma [35] proposed a MFE model for higher-order shear deformations of symmetrically FG beams considering both material and geometry variations through the section. Avcar et al. [36] employed higher-order shear deformation theory for sigmoid FG sandwich beams. Tran et al. [37] presented a finite element formulation based on a novel third-order shear deformation theory for FG sandwich beams in high-temperature environment. Ruocco and Reddy [38] compared the generalized stress/strain and corresponding local quantities of classical, first-order and third-order shear deformation theories. Le et al. [39] derived a third-order shear deformation beam element for the natural frequencies and buckling of bi-directional FG sandwich beams. Belarbi et al. [40] developed a 2-node finite element based on a novel parabolic shear deformation theory for FG sandwich beams. Czekanski and Zozulya [41] investigated the dynamic behaviors of shear deformable beams compared to the classical theories. Choi and Kim [42] presented a novel higher-order shear deformable beam theory that provides explicit stress-generalized force relations. Zhang et al. [43] investigates the stability of higher-order shear deformable beams under thermal effects via two well-posed nonlocal elasticity theories. Ziou et al. [44] proposed a polynomial higher-order shear deformation theory for FG beams.

Despite of many researchers derived higher-order shear deformable beam theories to consider the distribution of shear stress through the thickness of FG beams, there is a limited work in the literature for FG curved beams. Belarbi et al. [45] developed a 2-node finite element model based on a novel higher-order shear deformation theory for the bending of FG sandwich thick–thin beams curved in elevation. Pei and Li [46] studied FG curved beams by using higher-order beam theory. Sayyad and Ghugal [47] presented a sinusoidal beam theory for the bending of FG sandwich beams curved in elevation. Karami et al. [48] employed a higher-order shear deformation theory to investigate the nonlocal buckling response of FG carbon nanotube reinforced composite curved beams. Belarbi et al. [49] developed a 2-node finite beam element based on a novel three-unknown refined shear theory for the stability of FG sandwich curved thick–thin beams. Lezgy-Nazargah et al. [50] presented the assessment of the four-variable refined shear deformation theory for the dynamic responses of curved sandwich beams. Fariborz and Batra [51] investigated the natural frequencies of bi-directional FG circular beams via a shear deformation theory. Javani et al. [52] studied the free vibration characteristics of thick FG deep arches via the unconstrained higher-order shear deformation theory. Avhad and Sayyad [53–55] proposed a higher-order shear and normal deformation theory for static, free vibration and thermal analyses of FG beams curved in elevation. Tran Thi Thu [56] studied the dynamic behavior of bi-directional FG curved nanobeams via the higher-order shear deformation theory. Aribas et al. [57] presented a warping included MFE formulation for the static and stress analyses of FG exact curved beams.

1.2 Aim and scope

There is no publication available on the higher-order stress distributions of FG spatial/planar exact curved beams subjected to out-of-plane loads as far as the author is aware. Within this scope, the coupling of bending-extension should be taken into consideration in addition to the warping displacements of non-circular cross sections [58–63]. This study proposes a two-noded exact curved mixed FE including higher-order shear deformation functions (HSDFs) in both normal and binormal directions. The developed two-noded curved mixed FE has twenty-eight degrees of freedom (DOFs) in total. The axis geometry is derived based on the exact functions of the gradient of arch length and curvature [64]. The volume fraction of FGM constituents is designed according to the power-law distribution and the rule of mixture. As another distinctive feature of this study, an accuracy element at supports, where the stress concentration occurs, is introduced to achieve more precise results. The normal and shear stress distributions through the thickness are derived based on the curvatures on the cross section and the stress equilibrium condition, respectively. The two-noded curved mixed FEs present quite satisfactory results with lesser degrees of freedom compared to the solid finite elements. The accurate and effective bi-directional higher-order shear deformation functions (BDHSDFs) and the settlement of accuracy elements are investigated in the numerical solution.

2 Theorical formulations

2.1 Functionally graded materials

The volume fraction of FGM constituents through the thickness of section is considered via equally divided fifty-layer partitions for linear variations. In the case of nonlinear variations, the layer partitions, whose absolute differences of the material properties on the top and bottom are greater than the respective absolute difference of linear variation, are also subdivided by the ratio of these two differences. The effective material properties, P_{eff}, are evaluated through the application of the rule of mixture and power-law volume fraction [65],

$$P_{\text{eff}}(b) = P_{\text{bot}} + \left(P_{\text{top}} - P_{\text{bot}}\right)\left(\frac{1}{2} + \frac{b}{h}\right)^{p} \tag{1}$$

where P presents the material properties such as Young's modulus E and Poisson's ratio ν, subscripts "bot" and "top" denote the bottom and top surfaces of the beam, respectively, p is the power-law index, h is the thickness of section and b is the binormal unit vector of Frenet coordinate.

2.2 Displacement and strain fields

Letting tangent, normal and binormal unit vectors are Frenet coordinates (t, n, b), the displacements in the beam continuum $\left(u_t^*, u_n^*, u_b^*\right)$ are enriched in this study by introducing the higher-order variations of shear deformations through the both n and b axes as follows (Fig. 1)

$$\begin{aligned} u_t^* &= u_t - \left(b - b_c\right) u_{b,t} + f_i(b)\,\varphi_n - \left(n - n_c\right) u_{n,t} + f_j(n)\varphi_b \\ u_n^* &= u_n - b\,\Omega_t \qquad ; \qquad u_b^* = u_b + n\,\Omega_t \end{aligned} \tag{2}$$

where the partial derivations are denoted by the commas in the subscripts, u_t, u_n, u_b are the displacements on the beam axis, Ω_t is the axial rotation and φ_n, φ_b are the shear rotations, $f_i(b)$ and $f_j(n)$ are the higher-order displacement functions in the direction of b and n, respectively and i,j are the function numbers.

The contribution of components $u_{b,t}$ and $u_{n,t}$ to u_t^* are defined over the neutral axis as reference via b_c and n_c,

$$b_c = \frac{\sum_{L=1}^{N}\left(b_L E_L A_L\right)}{\sum_{L=1}^{N}\left(E_L A_L\right)} \; ; \; n_c = \frac{\sum_{L=1}^{N}\left(n_L E_L A_L\right)}{\sum_{L=1}^{N}\left(E_L A_L\right)} \tag{3}$$

where b_L, n_L and A_L are the geometric centers and cross sectional area of the layer partition L, respectively, and N is the total number of the layer partitions. Thus, the strain components can be derived as,

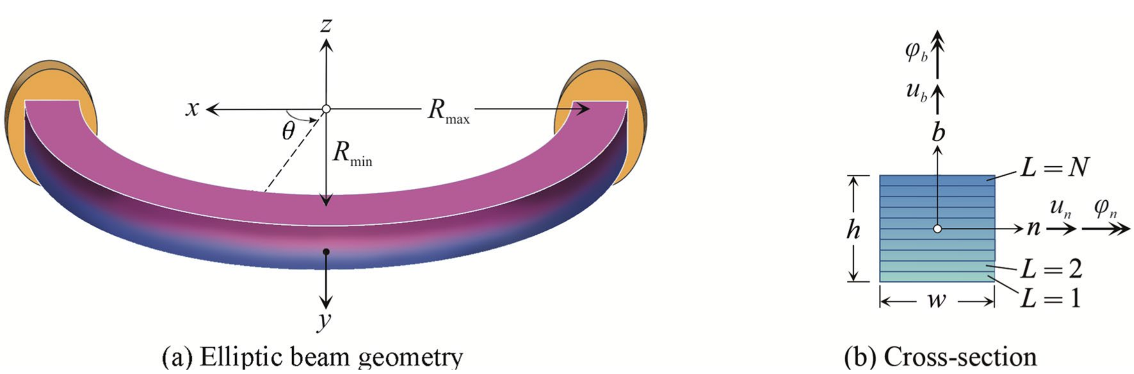

Fig. 1 Geometry and boundary conditions (**a**) and TFG cross section (**b**)

$$\varepsilon_t = u_{t,t} - \left(b - b_c\right) u_{b,tt} + f_i(b)\varphi_{n,t} - \left(n - n_c\right) u_{n,tt} + f_j(n)\varphi_{b,t}$$
$$\gamma_{bt} = f_{i,b}(b)\,\varphi_n + n\,\Omega_{t,t}$$
$$\gamma_{tn} = f_{j,n}(n)\varphi_b - b\,\Omega_{t,t} \tag{4}$$

The viability and effectiveness of the bi-directional higher-order shear deformable formulation are studied by implementing several higher-order displacement functions (Table 1) into Eq. (4) in the scope of this paper. However, the presented formulation can be used via implementing any higher-order shear deformation functions (HSDFs) in the bi-normal direction b and/or normal direction n. HSDFs $f_i(b)$ and $f_j(n)$, which are implemented in the directions of b and n in Eq. (4), are denoted by HSDT$_{ij}$ where the subscripts i and j present the functions (Table 1) in the direction b and n, respectively. The first derivatives of these HSDFs are presented graphically in Fig. 2 through the normalized thickness $\overline{b} = b/h$.

2.3 Constitutive equations

Based on the generalized Hooke's law [71], the constitutive equations that satisfy the stress-free surface conditions $\sigma_n = \sigma_b = \tau_{nb} = 0$ [59, 61] and bi-directional higher-order stress deformations are,

$$\begin{Bmatrix} \sigma_t \\ \tau_{bt} \\ \tau_{tn} \end{Bmatrix}_L = \boldsymbol{\beta}_L \begin{Bmatrix} \varepsilon_t \\ \gamma_{bt} \\ \gamma_{tn} \end{Bmatrix}_L = \begin{bmatrix} \beta_{11} & 0 & \beta_{13} \\ 0 & \beta_{22} & 0 \\ \beta_{13} & 0 & \beta_{33} \end{bmatrix}_L \mathbf{Z} \begin{Bmatrix} \mathbf{e}_F \\ \mathbf{e}_M \\ \mathbf{e}_h \end{Bmatrix} \tag{5}$$

where $\mathbf{e}_F = \left\{ u_{t,t}\ \varphi_b\ \varphi_n \right\}^{\mathrm{T}}$, $\mathbf{e}_M = \left\{ \Omega_{t,t}\ -u_{b,tt}\ u_{n,tt} \right\}^{\mathrm{T}}$, $\mathbf{e}_h = \left\{ \varphi_{n,t}\ \varphi_{b,t} \right\}^{\mathrm{T}}$ and L presents a layer partition. Thus, the internal forces $\mathbf{F} = \left\{ F_t\ F_n\ F_b \right\}^{\mathrm{T}}$, moments $\mathbf{M} = \left\{ M_t\ M_n\ M_b \right\}^{\mathrm{T}}$ and higher-order moments $\mathbf{M}^h = \left\{ M_n^h\ M_b^h \right\}^{\mathrm{T}}$ can be expressed by the integration of stresses as,

$$\begin{Bmatrix} \mathbf{F} \\ \mathbf{M} \\ \mathbf{M}^h \end{Bmatrix} = \sum_{L=1}^{N} \left(\int_{A_L} \mathbf{Z}^T\, \boldsymbol{\beta}_L\, \mathbf{Z}\, dA_L \right) \begin{Bmatrix} \mathbf{e}_F \\ \mathbf{e}_M \\ \mathbf{e}_h \end{Bmatrix} = \mathbf{E} \begin{Bmatrix} \mathbf{e}_F \\ \mathbf{e}_M \\ \mathbf{e}_h \end{Bmatrix} \tag{6}$$

Referring to the elasticity matrix $\boldsymbol{E}$, the compliance matrix can be defined as $\mathbf{C} = \mathbf{E}^{-1}$.

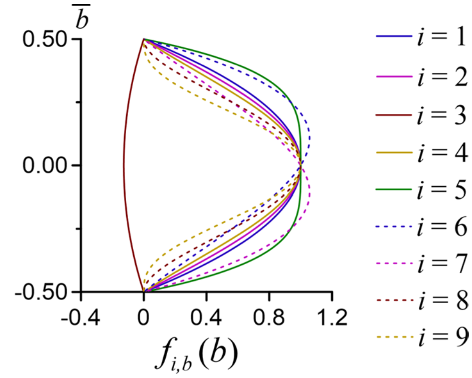

Fig. 2 First derivatives of HSDFs $f_{i,b}(b)$ through the thickness (Table 1)

2.4 Field equations, functional and mixed finite element

The equilibrium equations of TFG exact curved beams can be expressed as,

Table 1 Higher-order displacement functions (w: width and h: thickness)

i,j	Reference	$f_i(b)$	$f_j(n)$
1	[66]	$b - \frac{4b^3}{3h^2}$	$n - \frac{4n^3}{3w^2}$
2	[67]	$\frac{h}{\pi} \sin\left(\frac{\pi b}{h}\right)$	$\frac{w}{\pi} \sin\left(\frac{\pi n}{w}\right)$
3	[68]	$h \sinh\left(\frac{b}{h}\right) - b \cosh\left(\frac{1}{2}\right)$	$w \sinh\left(\frac{n}{w}\right) - n \cosh\left(\frac{1}{2}\right)$
4	[69]	$b\, 3^{-2(b/h)^2/\ln 3}$	$n\, 3^{-2(n/w)^2/\ln 3}$
5	[70]	$b - \left(\frac{16b^5}{5h^4}\right)$	$n - \left(\frac{16n^5}{5w^4}\right)$
6	[70]	$b + \left(\frac{b^2}{2h}\right) - \left(\frac{4b^3}{3h^2}\right) - \left(\frac{b^4}{h^3}\right)$	$n + \left(\frac{n^2}{2w}\right) - \left(\frac{4n^3}{3w^2}\right) - \left(\frac{n^4}{w^3}\right)$
7	[70]	$b - \left(\frac{b^2}{2h}\right) - \left(\frac{4b^3}{3h^2}\right) + \left(\frac{b^4}{h^3}\right)$	$n - \left(\frac{n^2}{2w}\right) - \left(\frac{4n^3}{3w^2}\right) + \left(\frac{n^4}{w^3}\right)$
8	[70]	$b - \left(\frac{8b^3}{3h^2}\right) + \left(\frac{16b^5}{5h^4}\right)$	$n - \left(\frac{8n^3}{3w^2}\right) + \left(\frac{16n^5}{5w^4}\right)$
9	[70]	$b - \left(\frac{4b^3}{h^2}\right) + \left(\frac{48b^5}{5h^4}\right) - \left(\frac{64b^7}{7h^6}\right)$	$n - \left(\frac{4n^3}{w^2}\right) + \left(\frac{48n^5}{5w^4}\right) - \left(\frac{64n^7}{7w^6}\right)$

$$\left\{\begin{array}{c} -F_{t,s} \\ M_{b,ss} \\ -M_{n,ss} \end{array}\right\} - \left\{\begin{array}{c} q_t \\ q_n \\ q_b \end{array}\right\} = \mathbf{0} \;\; ; \;\; -\left\{\begin{array}{c} M_{t,s} \\ M^h_{n,s} \\ M^h_{b,s} \end{array}\right\} + \left\{\begin{array}{c} 0 \\ F_b \\ F_n \end{array}\right\} - \left\{\begin{array}{c} m_t \\ m_n \\ m_b \end{array}\right\} = \mathbf{0} \tag{7}$$

where $\mathbf{q} = \left\{ q_t \; q_n \; q_b \right\}^{\mathrm{T}}$ and $\mathbf{m} = \left\{ m_t \; m_n \; m_b \right\}^{\mathrm{T}}$ are the external distributed force and moment vectors, respectively, s is the axial arc length. The constitutive equations can also be expressed as,

$$-\mathbf{C}\left\{\begin{array}{c} \mathbf{F} \\ \mathbf{M} \\ \mathbf{M}^h \end{array}\right\} + \left\{\begin{array}{c} \mathbf{e}_F \\ \mathbf{e}_M \\ \mathbf{e}_h \end{array}\right\} = \mathbf{0} \tag{8}$$

The field equations [72, 73] are enhanced by employing the higher-order shear deformation functions on the equilibrium equations (Eq. (7)) and the constitutive equations (Eq. (8)). Then the functional is derived over the field equations via the Hellinger Reissner principle as follows,

2.5 The stresses

The normal stress is derived from the constitutive equations via the respective curvatures in Eq. (5). However, the shear stress is obtained from the equilibrium conditions of beam segments which contain the respective nodes (Fig. 3) as $\tau_{bt} = \int \left(\Delta\sigma_t \,\mathrm{d}b\right) / 0.05\left(s_e + s_{e-1}\right)$ where e denotes the element number. The incremental normal stress $\Delta\sigma_t$ is determined from Eqns. (5) and (6) as follows,

$$\left\{\begin{array}{c} \Delta\sigma_t \\ \Delta\tau_{bt} \\ \Delta\tau_{tn} \end{array}\right\}_L = \boldsymbol{\beta}_L \mathbf{Z}\,\mathbf{C}\,\Phi\left(\left\{\begin{array}{c} \mathbf{F} \\ \mathbf{M} \\ \mathbf{M}^h \end{array}\right\}_{i+1} - \left\{\begin{array}{c} \mathbf{F} \\ \mathbf{M} \\ \mathbf{M}^h \end{array}\right\}_{i-1}\right) \tag{10}$$

where $\Phi = \left(\theta - \theta_i\right) / \left(\theta_{i+1} - \theta_i\right)$, i and $\theta = 0.05\theta_{i+1} + 0.95\theta_i$ indicate the node number and the central arc length angle, respectively.

3 Numerical solutions

$$\begin{aligned} I_{[y]} = & -\left[F_{t,s}, u_t\right] - \left[M_{b,s}, u_{n,s}\right] + \left[M_{n,s}, u_{b,s}\right] - \left[M_{t,s}, \Omega_t\right] - \left[M^h_{n,s}, \varphi_n\right] + \left[F_b, \varphi_n\right] - \left[M^h_{b,s}, \varphi_b\right] + \left[F_n, \varphi_b\right] \\ & - \tfrac{1}{2}\left[C_{11}F_t, F_t\right] - \tfrac{1}{2}\left[C_{12}F_n, F_t\right] - \tfrac{1}{2}\left[C_{14}M_t, F_t\right] - \tfrac{1}{2}\left[C_{15}M_n, F_t\right] - \tfrac{1}{2}\left[C_{17}M^h_n, F_t\right] \\ & - \tfrac{1}{2}\left[C_{21}F_t, F_n\right] - \tfrac{1}{2}\left[C_{22}F_n, F_n\right] - \tfrac{1}{2}\left[C_{24}M_t, F_n\right] - \tfrac{1}{2}\left[C_{25}M_n, F_n\right] - \tfrac{1}{2}\left[C_{27}M^h_n, F_n\right] - \tfrac{1}{2}\left[C_{33}F_b, F_b\right] \\ & - \tfrac{1}{2}\left[C_{41}F_t, M_t\right] - \tfrac{1}{2}\left[C_{42}F_n, M_t\right] - \tfrac{1}{2}\left[C_{44}M_t, M_t\right] - \tfrac{1}{2}\left[C_{45}M_n, M_t\right] - \tfrac{1}{2}\left[C_{47}M^h_n, M_t\right] \\ & - \tfrac{1}{2}\left[C_{51}F_t, M_n\right] - \tfrac{1}{2}\left[C_{52}F_n, M_n\right] - \tfrac{1}{2}\left[C_{54}M_t, M_n\right] - \tfrac{1}{2}\left[C_{55}M_n, M_n\right] - \tfrac{1}{2}\left[C_{57}M^h_n, M_n\right] \\ & - \tfrac{1}{2}\left[C_{66}M_b, M_b\right] - \tfrac{1}{2}\left[C_{68}M^h_b, M_b\right] - \tfrac{1}{2}\left[C_{86}M_b, M^h_b\right] - \tfrac{1}{2}\left[C_{88}M^h_b, M^h_b\right] \\ & - \tfrac{1}{2}\left[C_{71}F_t, M^h_n\right] - \tfrac{1}{2}\left[C_{72}F_n, M^h_n\right] - \tfrac{1}{2}\left[C_{74}M_t, M^h_n\right] - \tfrac{1}{2}\left[C_{75}M_n, M^h_n\right] - \tfrac{1}{2}\left[C_{77}M^h_n, M^h_n\right] \\ & - \left[q_t, u_t\right] - \left[q_n, u_n\right] - \left[q_b, u_b\right] - \left[m_t, \Omega_t\right] - \left[m_n, \varphi_n\right] - \left[m_b, \varphi_b\right] + \tfrac{1}{2}\left\langle M_{b,s}, u_n\right\rangle_O + \tfrac{1}{2}\left\langle M_{n,s}, u_b\right\rangle_O \\ & + \left\langle F_t - \widehat{F}_t, u_t\right\rangle_\sigma + \left\langle M_t - \widehat{M}_t, \Omega_t\right\rangle_\sigma - \left\langle M_n - \widehat{M}_n, u_{b,s}\right\rangle_\sigma + \left\langle M_b - \widehat{M}_b, u_{n,s}\right\rangle_\sigma \\ & - \left\langle M^h_n - \widehat{M}^h_n, \varphi_n\right\rangle_\sigma - \left\langle M^h_b - \widehat{M}^h_b, \varphi_b\right\rangle_\sigma + \left\langle \widehat{u}_t, F_t\right\rangle_\varepsilon - \left\langle \widehat{\varphi}_n, M^h_n\right\rangle_\varepsilon - \left\langle \widehat{\varphi}_b, M^h_b\right\rangle_\varepsilon \\ & + \left\langle \widehat{\Omega}_t, M_t\right\rangle_\varepsilon - \left\langle \widehat{u}_{b,s}, M_n\right\rangle_\varepsilon + \left\langle \widehat{u}_{n,s}, M_b\right\rangle_\varepsilon \end{aligned} \tag{9}$$

In Eq. (9), the dynamic (forced) and geometric (natural) boundary conditions are denoted by the subscripts σ and ε, respectively ($o = \sigma + \varepsilon$) and the terms with hats are known values on the boundary. Referring to Eq. (9), the two-noded curved mixed finite elements (MFEs) have fourteen nodal variables. The exact curved axial geometry is derived based on the procedure given in [74].

In Sect. 3.1, the appropriate degrees of freedoms (DOFs) that satisfy enough convergence for the normal/shear stress components of transversely functionally graded (TFG) exact curved beams are determined using 20-node solid FEs of ANSYS (60 DOFs) and 2-node mixed FEs (28 DOFs). In Sect. 3.2.1, an accuracy element is introduced to achieve more precise variation of normal/shear stress components that are influenced

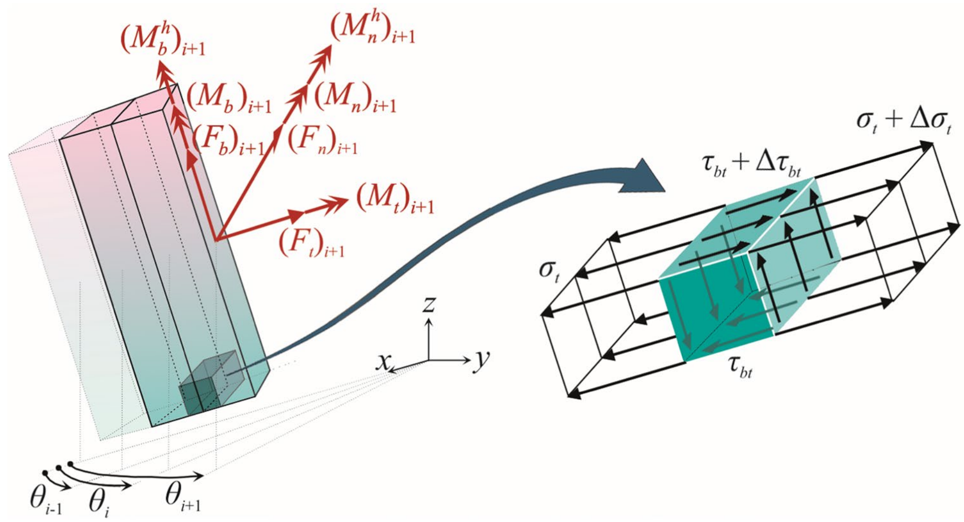

Fig. 3 Stress equilibrium condition of a layer partition for τ_{bt}

from stress concentrations through the clamped ends. In Sect. 3.2.2, bi-directional higher-order shear deformation functions (BDHSDFs) are utilized on predicting the normal/shear stress components due to the radius-to-thickness ratio. Higher-order shear deformation functions (HSDFs) which are employed in the binormal and normal directions are denoted by HSDT_{ij} where i and j present the function numbers (Table 1) in the binormal and normal directions, respectively. Then in Sects. 3.2.3–3.2.5, the accuracy of the proposed formulation due to the curvature, FGM constituents and power-law index is presented. Finally, in Sect. 3.2.6, the influence of transverse HSDFs on the stress variation is evaluated on a TFG spatial curved beam.

In all numerical solutions, TFG planar curved beams (Fig. 1) have clamped–clamped supports (both ends have fixed boundary conditions) and the central arch length angle is $\theta = 180°$. The ellipticity ratio is set to $\Gamma = R_{\min}/R_{\max} = 1.0$, 0.9, 0.8 and 0.7 while keeping the maximum radius constant as $R_{\max} = 3.0\,\text{m}$. In each case of Γ, the radius-to-thickness ratio is set to $\lambda_s = R_{\max}/h = 5$, 10, 15, 20 and 25 where h is the thickness of the square cross section. TFG exact curved beams are subjected to a transverse uniformly distributed load $q = 0.5\,\text{kN/m}$ along the arc length. The material constants of FGM constituents are given in Table 2. The normal $\sigma\left(\bar{t},\bar{b}\right)$ and shear stresses $\tau\left(\bar{t},\bar{b}\right)$ are given along the normalized tangential coordinate $\bar{t} = t/S$, where S is the total axial arc length and the normalized thickness of cross section $\bar{b} = b/h$.

Table 2 FGM constituents in the numerical examples

	Young's Modulus	Poisson's Ratio
Material	E (GPa)	ν
Alumina (Al_2O_3)	380.00	0.30
Steel (St)	210.00	0.30
Copper (Cu)	110.00	0.34
Aluminum (Al)	70.00	0.30

3.1 The convergence analyses

FE mesh convergence analyses are performed for the ellipticity ratios $\Gamma = 1.0$ and 0.7 and the radius-to-thickness ratios $\lambda_s = 5$ and 25 for each Γ. The bottom and top surfaces of the TFG cross section are Al and Al_2O_3, respectively, where the power-law index is $p = 1$. The FE mesh convergence for the normal/shear stress components is performed on the cross section at first node next to the clamped end both for the MFEs and the solid FEs.

3.1.1 Mixed finite elements

The normal/shear stress components of MFEs, $\sigma(0.05, 0.5)$ and $\tau(0.05, 0)$, are presented graphically in Fig. 4 for 294, 854, 1414, 1974, 2534 and 3094 DOFs. In the case of $\lambda_s = 25$, the maximum percent difference of the results of 1414 DOFs with respect to the 3094 DOFs is obtained for $\Gamma = 0.7$, HSDT_{99} and $\tau(0.05, 0)$ as 0.18% (-0.1386MPa for 1414DOFs and -0.1383MPa for 3094DOFs). Similarly in the case of $\lambda_s = 5$, it is obtained for $\Gamma = 0.7$, HSDT_{33} and $\tau(0.05, 0)$ as 1.66% (-0.0047MPa for 1414DOFs and -0.0046MPa for 3094DOFs). The outcomes reveal that 1414 DOFs (100 mixed FEs) satisfy enough convergence. The advantage of mixed finite elements is that both the displacements and stress resultants are DOFs. Therefore, the precision is increased while saving time from overall computation period.

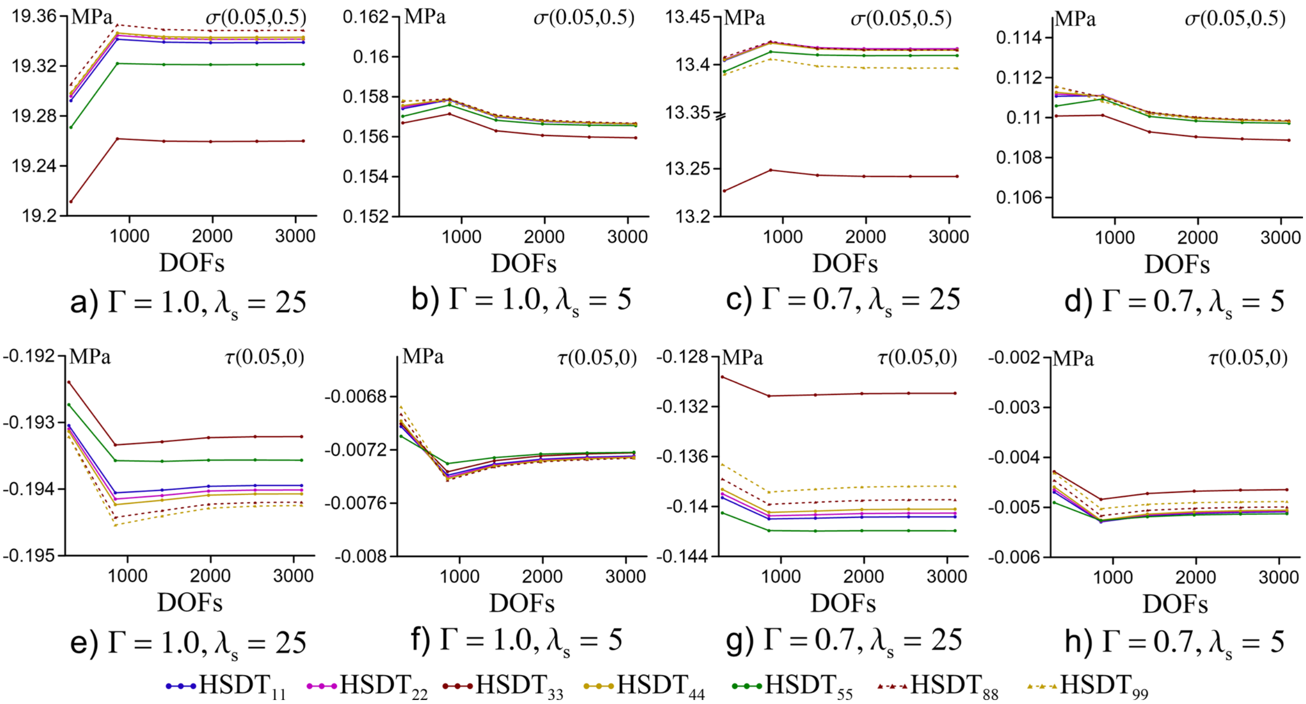

Fig. 4 FE mesh convergence for $\sigma(0.05, 0.5)$ and $\tau(0.05, 0)$ of MFEs

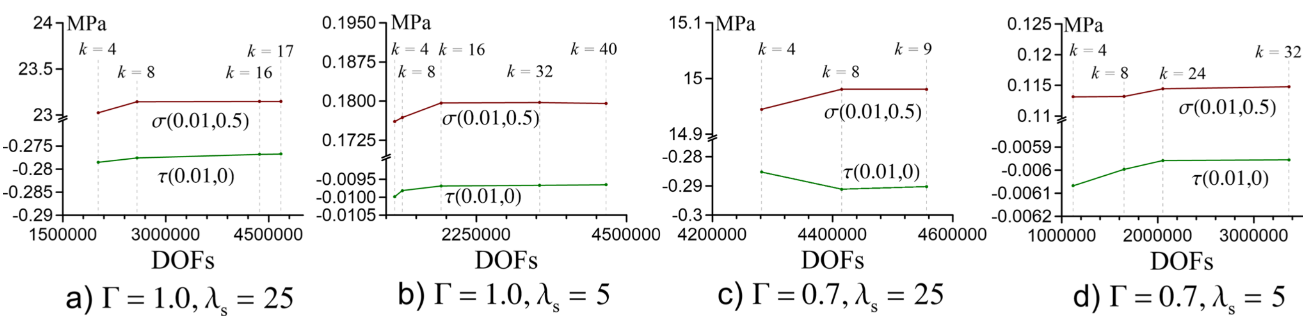

Fig. 5 FE mesh convergence of solid FEs for $\sigma(0.01, 0.5)$ and $\tau(0.01, 0)$

3.1.2 Solid finite elements

The solid geometry of TFG curved beam (circular and elliptical) is modeled using SOLID186 elements (solid FEs of ANSYS) based on the coordinates of nodal points of 200 mixed FE discretization. FE mesh convergence analysis is performed by defining the mesh element size as w/k, where w is the width of square section and $k = 4$ in the range of $0.05 < \bar{t} < 0.95$, afterward in the ranges of $\bar{t} \leq 0.05$ and $0.95 \leq \bar{t}$, body sizing is assigned for various k quantities successively. The normal/shear stress components of solid FEs, $\sigma(0.01, 0.5)$ and $\tau(0.01, 0)$, are presented graphically in Fig. 5.

In Fig. 5a, the percent difference of the results of $k = 16$ with respect to $k = 17$ is ~0.03%. In Fig. 5b, the percent differences of the results of $k = 32$ with respect to $k = 40$ are 0.09% for $\sigma(0.01, 0.5)$ and 0.15% for $\tau(0.01, 0)$. In Fig. 5c, the percent differences of the results of $k = 8$ with respect to $k = 9$ are 0.00% for $\sigma(0.01, 0.5)$ and 0.30% for $\tau(0.01, 0)$. In

Table 3 Quantity of k due to the ratios of ellipticity Γ and radius-to-thickness λ_s

Γ	$\lambda_s = 5$	10	15	20	25
1.0	32.00	28.00	24.00	20.00	16.00
0.9	29.33	25.33	21.33	12.50	10.90
0.8	26.67	22.67	18.67	14.67	10.67
0.7	24.00	20.00	16.00	12.00	8.00

Fig. 5d, the percent differences of the results of $k = 24$ with respect to $k = 32$ are -0.29% for $\sigma(0.01, 0.5)$ and 0.05% for $\tau(0.01, 0)$. By means of these results, the selected k quantities due to the geometric features of solid geometries in the following assessments are reported in Table 3.

3.2 The assessment of accuracy

In the first instance, an additional MFE (accuracy element) at each clamped end, where the stress concentration occurs, is placed to increase the precision of normal/shear stress variations. These elements' appropriate nodal coordinates that provide more precise results are specified over the central arch length angle (Sect. 3.2.1). The performance of BDHSDFs in predicting the abovementioned stresses is assessed with respect to the geometric and material features (Sects. 3.2.2–3.2.6). The influence of transverse HSDFs on the stresses is estimated on a TFG spatial curved beam which demonstrates greater coupling effects with respect to the planar curved beams. In all numerical solutions, the geometric and material features, loading and boundary conditions are as given in Sect. 3.

3.2.1 The accuracy element

This section specifies the appropriate nodal coordinates of accuracy elements over the central arch length angle θ which results more precise stress variations. The accuracy of normal/shear stress variations through the thickness is evaluated with respect to the results of solid FEs (SOLID186 elements of ANSYS). The stress variations are presented for various mesh refinements of accuracy MFEs by setting their unrestricted nodes successively to $\theta_{\mathrm{UN}} = 0.0002\theta, 0.0006\theta, 0.001\theta, 0.003\theta, 0.005\theta, 0.007\theta$, and 0.009θ. Referring to the geometric features and loading in Sect. 3, TFG semi-circular beam with $\Gamma = 1$ and $\lambda_s = 5$ is investigated. The bottom and top surfaces of TFG section are Al and Al_2O_3, respectively. The power-law index is $p = 1$.

Figure 6 demonstrates the variation of shear stress $\tau(\bar{t}, 0)$ through the clamped end graphically for various quantities of θ_{UN}. HSDT_{11}, HSDT_{22}, HSDT_{33}, HSDT_{44} and HSDT_{55} provide the absolute minimum percent difference of $\tau(0.05, 0)$ with respect to the solid FEs for $\theta_{\mathrm{UN}} = 0.008\theta$, 0.008θ, 0.005θ, 0.007θ and 0.009θ, respectively (Table 5). The absolute minimum/maximum percent differences of $\tau(0.05, 0)$ are obtained for HSDT_{11} and HSDT_{55}, respectively. As $\bar{t}$ decreases to 0.04, the percent difference of $\tau(0.04, 0)$ for the stated BDHSDFs with their corresponding θ_{UN} becomes at least -6.71%.

Since the absolute maximum percent difference of $\tau(0.05, 0)$ with respect to the solid FEs is obtained in the case of HSDT_{55} (Table 4), the through-thickness shear stresses $\tau\left(\bar{t}, \bar{b}\right)$ of HSDT_{55} and SOLID186 elements are given for $\bar{t} = 0.01$, 0.02, 0.03, 0.04 and 0.05 in Fig. 7. At $\bar{t} = 0.05$, the results are satisfactory independent from θ_{UN}. The percent differences of the maximum shear stress $\tau_{\max}\left(0.05, \bar{b}\right)$ obtained via $\theta_{\mathrm{UN}} = 0.009\theta$ with respect to the results of $\theta_{\mathrm{UN}} = 0.0006\theta$ and SOLID186 elements are -0.39 and -1.74%, respectively (Table 5). In addition to the increase in the influence of θ_{UN} on the results through the clamped end, the percent difference of the results compared to the solid FEs increases. The percent difference of $\tau_{\max}\left(0.01, \bar{b}\right)$

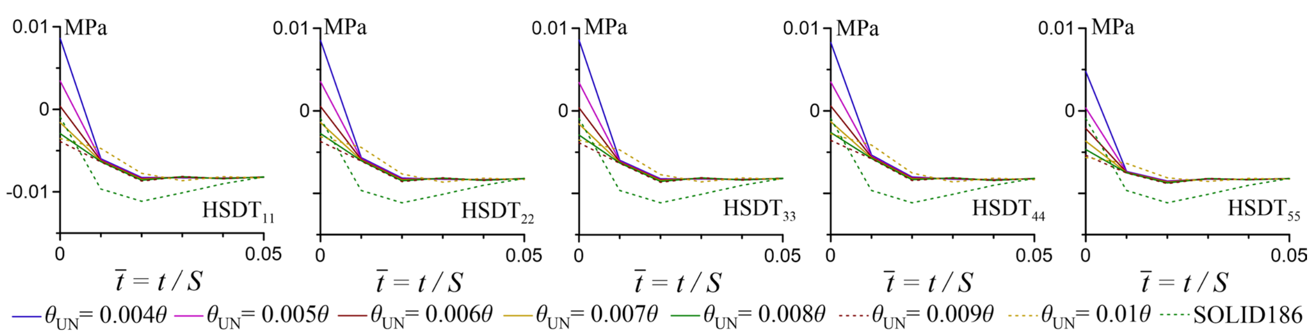

Fig. 6 Shear stress variations through the clamped end for θ_{UN}

Table 4 Shear stresses $\tau(\bar{t}, 0)$ in kPa at $\bar{t} = 0.05$ and 0.04 (Fig. 6). Diff.% = 100× $[(\tau(\bar{t}, 0)/\mathrm{SOLID186}) - 1]$

	$\bar{t}$	HSDT_{11}	HSDT_{22}	HSDT_{33}	HSDT_{44}	HSDT_{55}	SOLID186
$\tau(\bar{t}, 0)$	0.05	−8.181	−8.178	−8.181	−8.185	−8.189	−8.180
	0.04	−8.388	−8.399	−8.308	−8.388	−8.329	−9.002
Diff.%	0.05	0.00%	−0.03%	−0.01%	−0.06%	−0.10%	
	0.04	−6.83%	−6.71%	−7.71%	−6.82%	−7.48%	

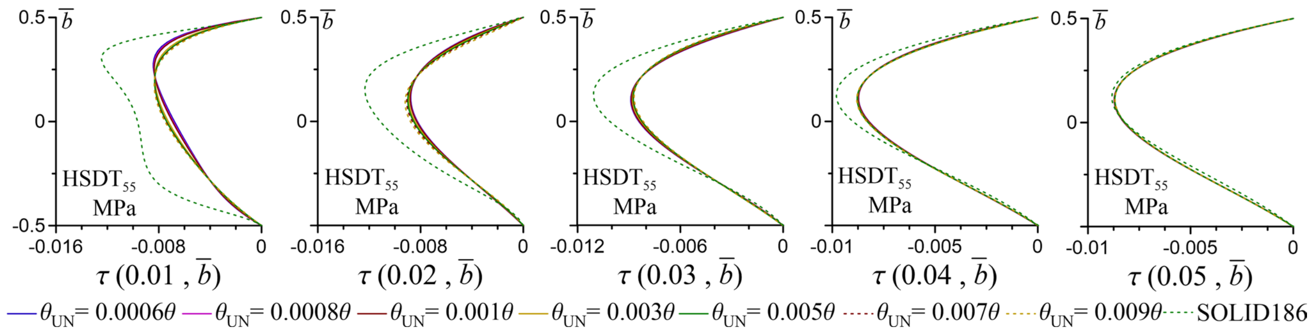

Fig. 7 Through-thickness shear stresses $\tau\left(\bar{t},\bar{b}\right)$ of HSDT$_{55}$

Table 5 Maximum shear stress $\tau_{\max}\left(\bar{t},\bar{b}\right)$ of HSDT$_{55}$ in kPa (Fig. 7)

$\bar{t}$	$\bar{b}$	SOLID186	θ_{UN}	
			0.009θ	0.0006θ
0.05	0.12	− 8.838	− 8.685	− 8.719
0.04	0.12	− 9.801	− 8.801	− 8.722
0.03	0.12	− 11.071	− 8.703	− 8.884
0.02	0.16	− 12.335	− 8.933	− 8.679
0.01	0.30	− 12.458	− 7.724	− 8.375

obtained via $\theta_{\mathrm{UN}} = 0.009\theta$ with respect to the result of $\theta_{\mathrm{UN}} = 0.0006\theta$ becomes -7.77%. However, the percent difference with respect to $\tau_{\max}\left(0.04,\bar{b}\right)$ of SOLID186 elements becomes -10.21% in the case of HSDT$_{55}$.

Figure 8 presents the through-thickness shear stresses $\tau\left(\bar{t},\bar{b}\right)$ of various BDHSDFs over $\theta_{\mathrm{UN}} = 0.009\theta$ at $\bar{t} = 0.01$, 0.02, 0.03, 0.04 and 0.05 compared to the solid FEs. Similar to the conclusions of HSDT$_{55}$, the influence of higher-order shear deformation functions on the results increases through

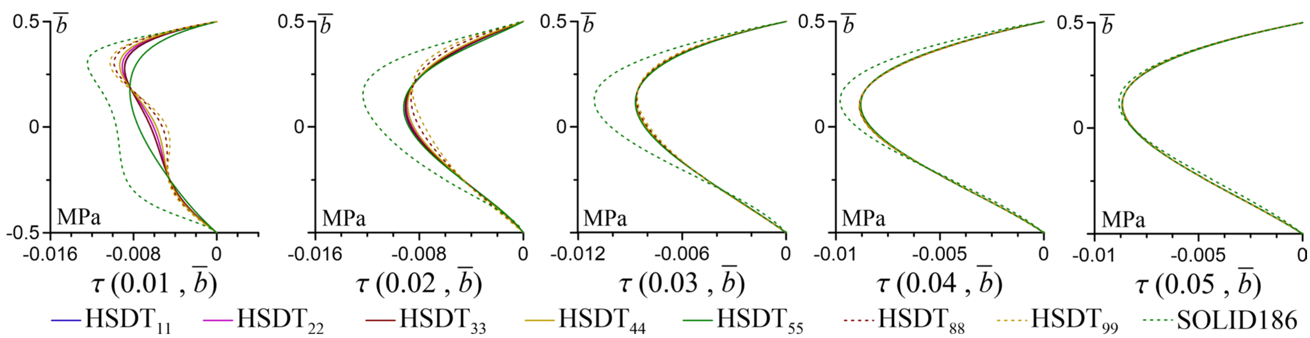

Fig. 8 Through-thickness shear stresses $\tau\left(\bar{t},\bar{b}\right)$ for various BDHSDFs

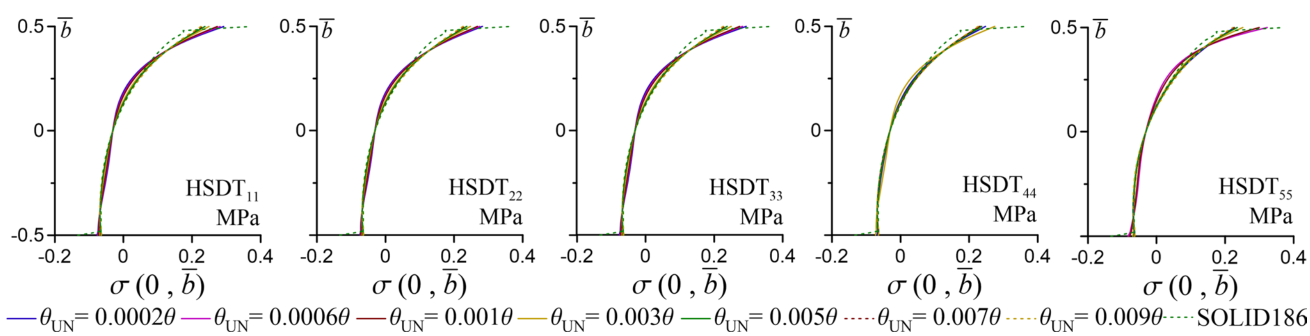

Fig. 9 Through-thickness normal stresses $\sigma\left(\bar{t},\bar{b}\right)$ at the clamped end

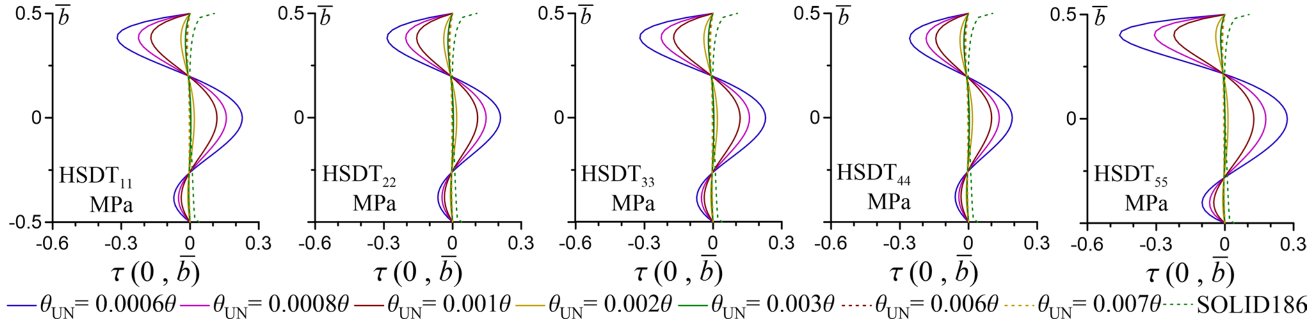

Fig. 10 Through-thickness shear stresses $\tau\left(\bar{t},\bar{b}\right)$ at the clamped end

the clamped end. As $\bar{t}$ decreases from 0.05 $\left(\bar{b}=0.12\right)$ to 0.01 $\left(\bar{b}=0.30\right)$, the percent difference of $\tau_{\max}\left(\bar{t},\bar{b}\right)$ obtained via $HSDT_{99}$ with respect to the results of $HSDT_{55}$ (Table 5) increases from -0.224% (-8.666kPa for $HSDT_{99}$) to 32.92% (-10.267kPa for $HSDT_{99}$). Besides, the percent difference of $\tau_{\max}\left(\bar{t},\bar{b}\right)$ obtained via $HSDT_{99}$ with respect to the solid FEs becomes -17.59% at $\bar{t}=0.01$.

The through-thickness normal/shear stress components at the clamped end are assessed due to various BDHSDFs and θ_{UN} in Figs. 9 and 10. The maximum/minimum influences of θ_{UN} on the maximum normal stress $\sigma_{\max}(0,0.50)$ are obtained in the cases of $HSDT_{55}$ and $HSDT_{44}$, respectively (Fig. 9). The maximum normal stresses $\sigma_{\max}(0,0.50)$ obtained via $\theta_{UN}=0.0002\theta$ and 0.009θ are 0.323MPa and 0.222MPa, respectively in the case of $HSDT_{55}$, and 0.275MPa and 0.227MPa, respectively in the case of $HSDT_{44}$. The percent differences of $\sigma_{\max}(0,0.50)$ obtained via $\theta_{UN}=0.0002\theta$ with respect to $\theta_{UN}=0.009\theta$ are 62.26% and 21.31% in the cases of $HSDT_{55}$ and $HSDT_{44}$, respectively. The decrease in θ_{UN} increases the precision of $\sigma_{\max}(0,0.50)$ more in the case of $HSDT_{55}$. The percent difference of $\sigma_{\max}(0,0.50)$ with respect to the solid FEs becomes -2.94% (0.372MPa for SOLID186 elements). However, it is -26.06% in the case of $HSDT_{44}$ and $\theta_{UN}=0.0002\theta$. At the clamped end, the shear stress $\tau(0,0.50)$ of SOLID186 elements becomes 0.106MPa where the stress-free conditions are valid for HSDFs (Fig. 10).

3.2.2 The radius-to-thickness ratio

Firstly, the influence of decrease in the radius-to-thickness ratio λ_s on the capability of θ_{UN} to provide accurate stress variations for BDHSDFs is investigated with respect to the solid FEs. Next, the variations of shear stresses through the clamped end are given related to λ_s. Finally, the through-thickness normal/shear stress components of various BDHSDFs are presented as λ_s decreases. Referring to the geometric features and loading in Sect. 3, λ_s is set to 5, 10, 15, 20 and 25, respectively ($R=3.0$m and $\Gamma=1$). The FGM constituents at the bottom and top of the section are Al and Al_2O_3, respectively where $p=1$.

Due to the conclusions in Sect. 3.2.1 (Fig. 6 and Table 4), the influence of θ_{UN} on the precision of shear stresses is investigated for $HSDT_{55}$ as λ_s decreases (Fig. 11). Although the increment in the precision of $\tau\left(0.05,\bar{b}\right)$ is independent of θ_{UN} as stated in Sect. 3.2.1 (Fig. 7), an increase in θ_{UN} increases the precision of $\tau(0,0)$ as λ_s decreases (Fig. 11). The shear stresses $\tau(0.05,0)$ of solid FEs are -192kPa, -122kPa, -69kPa, -31kPa and -8kPa for $\lambda_s=25, 20, 15, 10$ and 5, respectively. As λ_s decreases from 25 to 5, the

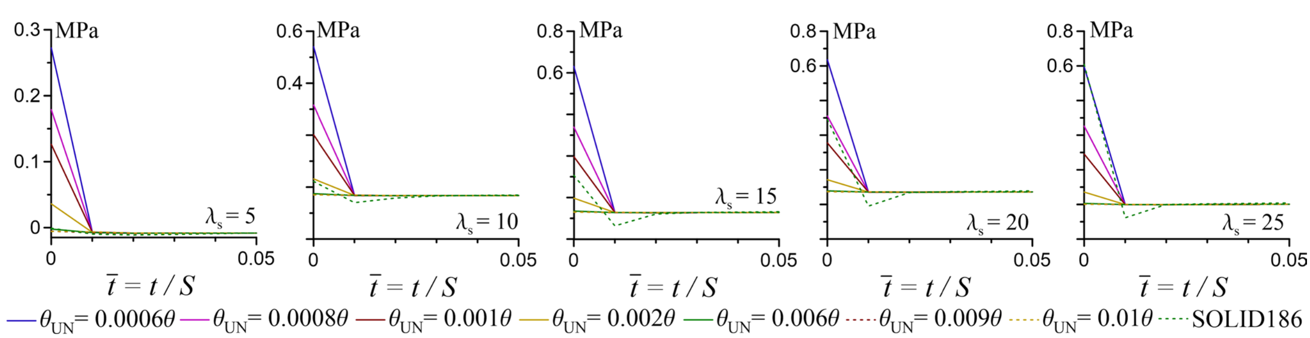

Fig. 11 Influence of θ_{UN} on the precision of $\tau\left(\bar{t},0\right)$ as λ_s decreases

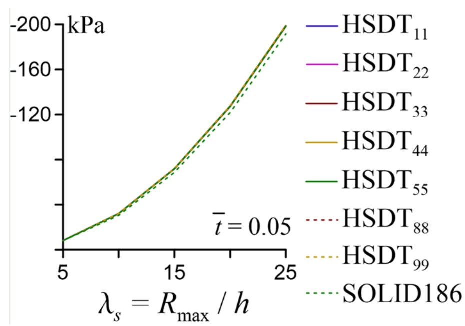

Fig. 12 Influence of λ_s on shear stress

percent difference of $\tau(0.05, 0)$ compared to solid FEs becomes 3.65% (-199kPa), 4.56% (-127kPa), 5.83% (-72kPa), 5.20% (-32kPa), 0.10% (-8kPa), respectively. Thus, the influence of λ_s on the shear stresses is investigated via $\theta_{UN} = 0.009\theta$ in this section.

Figure 12 presents the influence of λ_s on the shear stress at $\bar{t} = 0.05$. Since HSDT$_{11}$ provides the minimum percent difference of $\tau(0.05, 0)$ compared to the solid FEs in the case of $\lambda_s = 5$ (Table 4), the convergence of the results is given in Table 6 as λ_s increases. The absolute shear stresses of HSDT$_{11}$ are greater than SOLID186 elements except $\lambda_s = 5$. The maximum percent difference of $\tau(0.05, 0)$ compared to the solid FEs is obtained in the case of $\lambda_s = 10$. As λ_s increases, $\tau(0.05, 0)$ becomes 3.74, 8.39, 14.89 and 23.41 times greater than the result of $\lambda_s = 5$, respectively.

The increase in $\sigma\left(0, \bar{b}\right)$ through the top surface of solid FEs becomes greater as λ_s decreases (Fig. 13). $\sigma(0, 0.50)$ is 2.13 times greater than $\sigma(0, 0.48)$ in the case of $\lambda_s = 5$ (0.37MPa and 0.17MPa, respectively), whereas it is 1.71

Table 6 Shear stresses as λ_s decreases

Stress	$\bar{t}$	$\lambda_s =$	5	10	15	20	25
Shear (kPa)	0.05	SOLID186	−8.18	−30.57	−68.66	−121.77	−191.53
		HSDT$_{11}$	−8.17	−32.20	−71.98	−127.55	−198.88
		Diff.%	−0.08	5.32	4.84	4.74	3.84

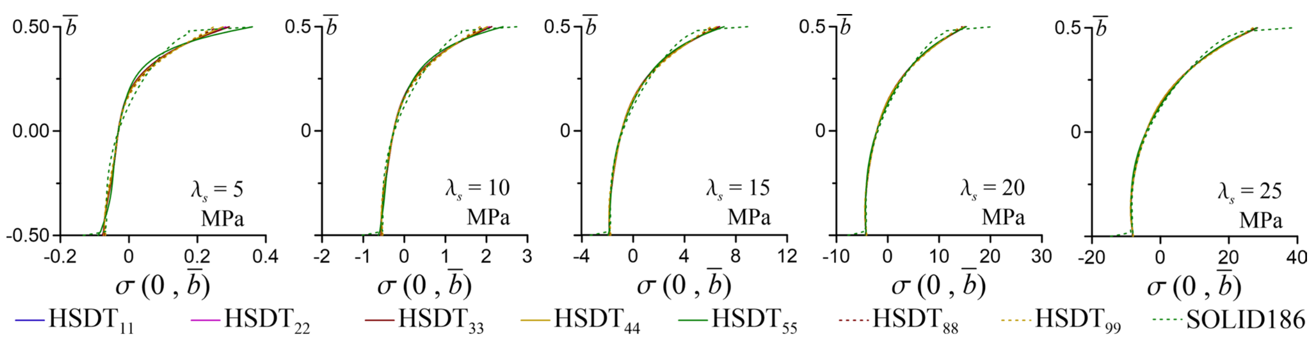

Fig. 13 Influence of λ_s on the through-thickness normal stress $\sigma\left(0, \bar{b}\right)$

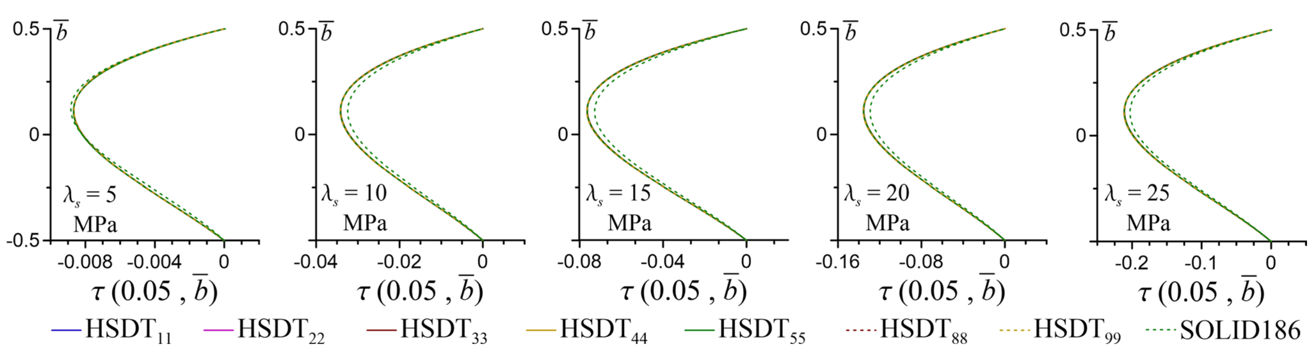

Fig. 14 Influence of λ_s on the through-thickness shear stresses

times greater than $\sigma(0, 0.48)$ in the case of $\lambda_s = 25$ (38.71MPa and 22.70MPa, respectively). The influence of decrease in λ_s on the rate of decrease in $\sigma(0, 0.50)$ becomes greater as λ_s decreases, $\sigma(0, 0.50)$ are 38.71MPa, 20.66MPa, 8.96MPa, 2.77MPa and 0.37MPa for $\lambda_s = 25$, 20, 15, 10 and 5, respectively. As λ_s decreases, the percent differences of $\sigma(0, 0.50)$ obtained via BDHSDFs compared to the results of solid FEs decrease except $HSDT_{88}$ and $HSDT_{99}$. $\tau_{\max}\left(0.05, \bar{b}\right)$ of solid FEs are − 202.94kPa, − 129.24kPa, − 72.80kPa, − 32.43kPa and − 8.84kPa for $\lambda_s = 25$, 20, 15, 10 and 5, respectively (Fig. 14). The influence of decrease in λ_s on the rate of decrease in $\tau_{\max}\left(0.05, \bar{b}\right)$ becomes greater as λ_s decreases. The minimum percent differences of $\tau_{\max}\left(0.05, \bar{b}\right)$ obtained via BDHSDFs compared to the solid FEs are 3.88% (− 210.81kPa), 4.59% (− 135.17kPa), 4.76% (− 76.27kPa), 5.13% (− 34.10kPa) and − 1.74% (− 8.68kPa), respectively, as λ_s decreases ($HSDT_{55}$ for $\lambda_s = 5$ and $HSDT_{33}$ for other λ_s). $\tau_{\max}\left(\bar{t}, \bar{b}\right)$ occurs closer to the top surface through the clamped end or as λ_s decreases (Figs. 8 and 14).

3.2.3 The ellipticity

The influence of ellipticity ratio ($\Gamma = R_{\min}/R_{\max}$) on the normal and shear stresses is presented in this section. Γ is set to 0.9, 0.8 and 0.7 successively for each $\lambda_s = R_{\max}/h = 5$, 10, 15, 20 and 25 referring to the geometric features and loading in Sect. 3 ($R_{\max} = 3.0$m). Based on the conclusions of Sects. 3.2.1–3.2.2, $\theta_{\mathrm{UN}} = 0.0002\theta$ and 0.009θ are used to determine the normal stress and shear stress, respectively. The FGM constituents are Al and Al_2O_3 at the bottom and top of the section, respectively ($p = 1$).

The relation between $\tau(0.05, 0)$ and Γ is presented in Fig. 15. In the cases of $\Gamma = 0.9$, 0.8 and 0.7, $\tau(0.05, 0)$ of solid FEs are − 7.89kPa, − 7.53kPa and − 7.05kPa for $\lambda_s = 5$, − 28.90kPa, − 26.90kPa and − 25.00kPa for $\lambda_s = 10$, − 64.80kPa, − 59.70kPa and − 55.20kPa for $\lambda_s = 15$, − 111.77kPa, − 104.68kPa and − 95.30kPa for $\lambda_s = 20$ and − 170.45kPa, − 159.09kPa and − 152.66kPa for $\lambda_s = 25$, respectively. The average percent decreases in $\tau(0.05, 0)$ of solid FEs are − 6.79%, − 6.48% and − 6.77% as Γ decreases between 1.0–0.9, 0.9–0.8 and 0.8–0.7, respectively. The shear stresses $\tau(0.05, 0)$ of BDHSDFs are obtained via $\theta_{\mathrm{UN}} = 0.0002\theta$ in the cases of $\Gamma = 0.7$ for each λ_s, and $\Gamma = 0.9$ and 0.8 for $\lambda_s = 5$. The absolute percent difference of $\tau(0.05, 0)$ compared to the solid FEs has a tendency of decreasing as Γ decreases except $HSDT_{33}$. However, it is quite opposite in the case of $\lambda_s = 5$.

The through-thickness $\sigma\left(0.05, \bar{b}\right)$ and $\tau\left(0.05, \bar{b}\right)$ are illustrated graphically as Γ decreases in Fig. 16. In the cases of $\Gamma = 1.0$, 0.9, 0.8 and 0.7, $\sigma_{\max}\left(0.05, \bar{b}\right)$ of solid FEs are 0.155MPa, 0.138MPa, 0.120MPa and 0.105MPa, respectively, for $\lambda_s = 5$ and 19.309MPa, 16.967MPa, 14.907MPa and 13.002MPa, respectively, for $\lambda_s = 25$. The corresponding percent decreases in $\sigma_{\max}\left(0.05, \bar{b}\right)$ are − 11.00%, − 12.47% and − 12.87% for $\lambda_s = 5$ and − 12.13%, − 12.14% and − 12.78% for $\lambda_s = 25$. As Γ decreases, its' influence on $\sigma_{\max}\left(0.05, \bar{b}\right)$ becomes greater. The percent difference of $\sigma_{\max}\left(0.05, \bar{b}\right)$ of BDHSDFs compared to solid FEs increases as Γ and/or λ_s decrease. In the case of $HSDT_{33}$, while it is − 0.26% (19.259MPa) for $\Gamma = 1.0$ and $\lambda_s = 25$, it increases to 1.85% (13.242MPa) as Γ decreases to 0.7 or it increases to 1.08% (0.155MPa) as λ_s decreases to 5. The maximum percent difference is obtained in the case of $\Gamma = 0.7$ and $\lambda_s = 5$ as 4.11% (0.105MPa).

The maximum shear stress $\tau_{\max}\left(0.05, \bar{b}\right)$ of solid FEs for $\Gamma = 1.0$, 0.9, 0.8 and 0.7 are successively − 8.84kPa, − 8.55kPa, − 8.14kPa and − 7.67kPa in the case of $\lambda_s = 5$, − 72.80kPa, − 68.67kPa, − 63.63kPa and − 58.45kPa in the case of $\lambda_s = 15$ and − 202.94kPa, − 180.55kPa, − 176.27kPa and − 161.52kPa in the case of $\lambda_s = 25$ (Fig. 16). As Γ decreases from 1.0 to 0.7 successively, the corresponding percent decreases in $\tau_{\max}\left(0.05, \bar{b}\right)$ becomes − 3.22%,

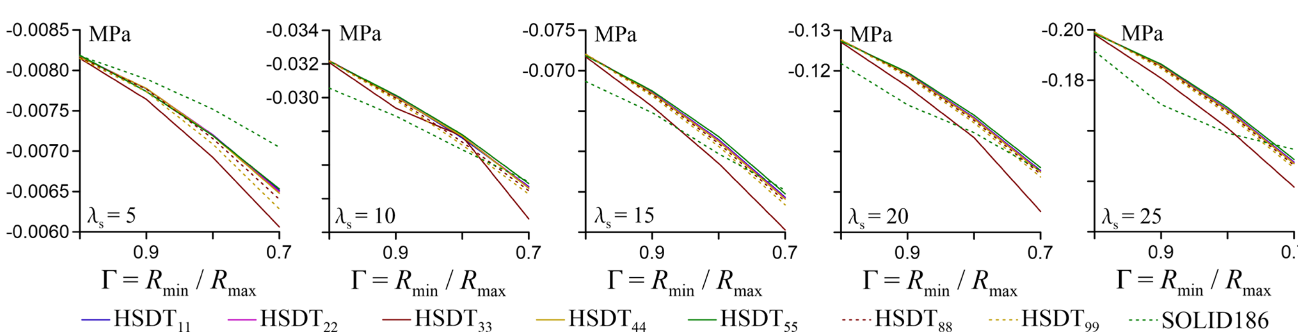

Fig. 15 Influence of Γ on the shear stress $\tau(0.05, 0)$

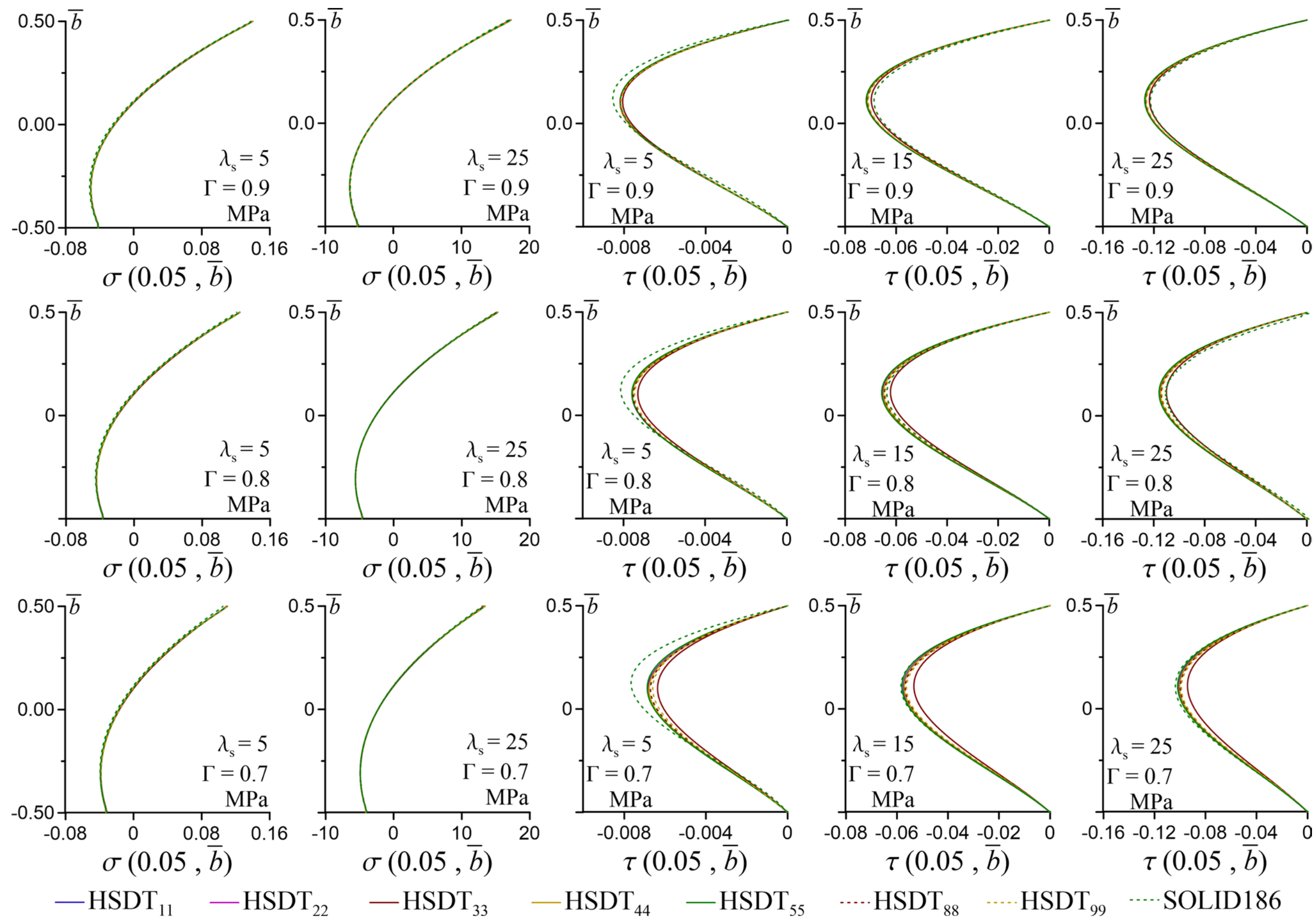

Fig. 16 Influence of Γ on the through-thickness $\sigma\left(0.05,\bar{b}\right)$ and $\tau\left(0.05,\bar{b}\right)$

-4.81% and -5.83% for $\lambda_s = 5$ and -5.68%, -7.34% and -8.14% for $\lambda_s = 15$. the influence of Γ on $\tau_{\max}\left(0.05,\bar{b}\right)$ becomes greater as Γ decreases except $\lambda_s = 25$. HSDT$_{55}$ converges better to $\tau_{\max}\left(0.05,\bar{b}\right)$ of solid FEs as Γ decreases in the scope of BDHSDFs. Although the convergence of HSDT$_{55}$ has a tendency of increasing as Γ decreases, it is quite the opposite for $\lambda_s = 5$. The percent difference of $\tau_{\max}\left(0.05,\bar{b}\right)$ compared to solid FEs decreases from -10.47% (-6.87kPa) to -4.32% (-8.18kPa) as Γ increases from 0.7 to 0.9 for $\lambda_s = 5$. However, it decreases from 9.73% (-198.12kPa) to -2.34% (-157.74kPa) as Γ decreases from 0.9 to 0.7 for $\lambda_s = 25$.

The through-thickness $\sigma\left(0,\bar{b}\right)$ at the clamped end is given as Γ decreases in Fig. 17. In the cases of Γ = 1.0, 0.9, 0.8 and 0.7, $\sigma_{\max}\left(0,\bar{b}\right)$ of solid FEs are 0.372MPa, 0.317MPa, 0.277MPa and 0.239MPa, respectively, for $\lambda_s = 5$ and 38.714MPa, 30.858MPa, 27.268MPa and 24.717MPa, respectively, for $\lambda_s = 25$. $\sigma_{\max}\left(0,\bar{b}\right)$ decreases as Γ and/or λ_s decrease. The increase rate of $\sigma_{\max}\left(\bar{t},\bar{b}\right)$ through the clamped end $\beta_t^{\sigma} = \sigma_{\max}\left(0,\bar{b}\right) / \sigma_{\max}\left(0.05,\bar{b}\right)$ is 1.90 for Γ = 0.7 and $\lambda_s = 25$. β_t^{σ} becomes greater as Γ increases and/or λ_s decreases. It increases to 2.01 as Γ increases to 1.0 or it increases to 2.28 as λ_s decreases to 5. HSDT$_{55}$ converges better to $\sigma_{\max}\left(0,\bar{b}\right)$ of solid FEs in the scope of BDHSDFs. However, in the case of HSDT$_{55}$ and $\theta_{UN} = 0.009\theta$, the percent differences compared to solid FEs becomes -14.23%, -11.49% and -7.91% for $\lambda_s = 5$ and -17.64%, -17.13% and -19.45% for $\lambda_s = 25$ in the cases of Γ = 0.9, 0.8 and 0.7, respectively.

3.2.4 FGM constituents

This section aims to present the influence of FGM constituents on the normal/shear stress components of TFG exact curved beams. Based on the conclusions of Sects. 3.2.1–3.2.2, the normal and shear stresses of BDHSDFs are obtained via $\theta_{\mathrm{UN}} = 0.0002\theta$ and $\theta_{\mathrm{UN}} = 0.009\theta$,

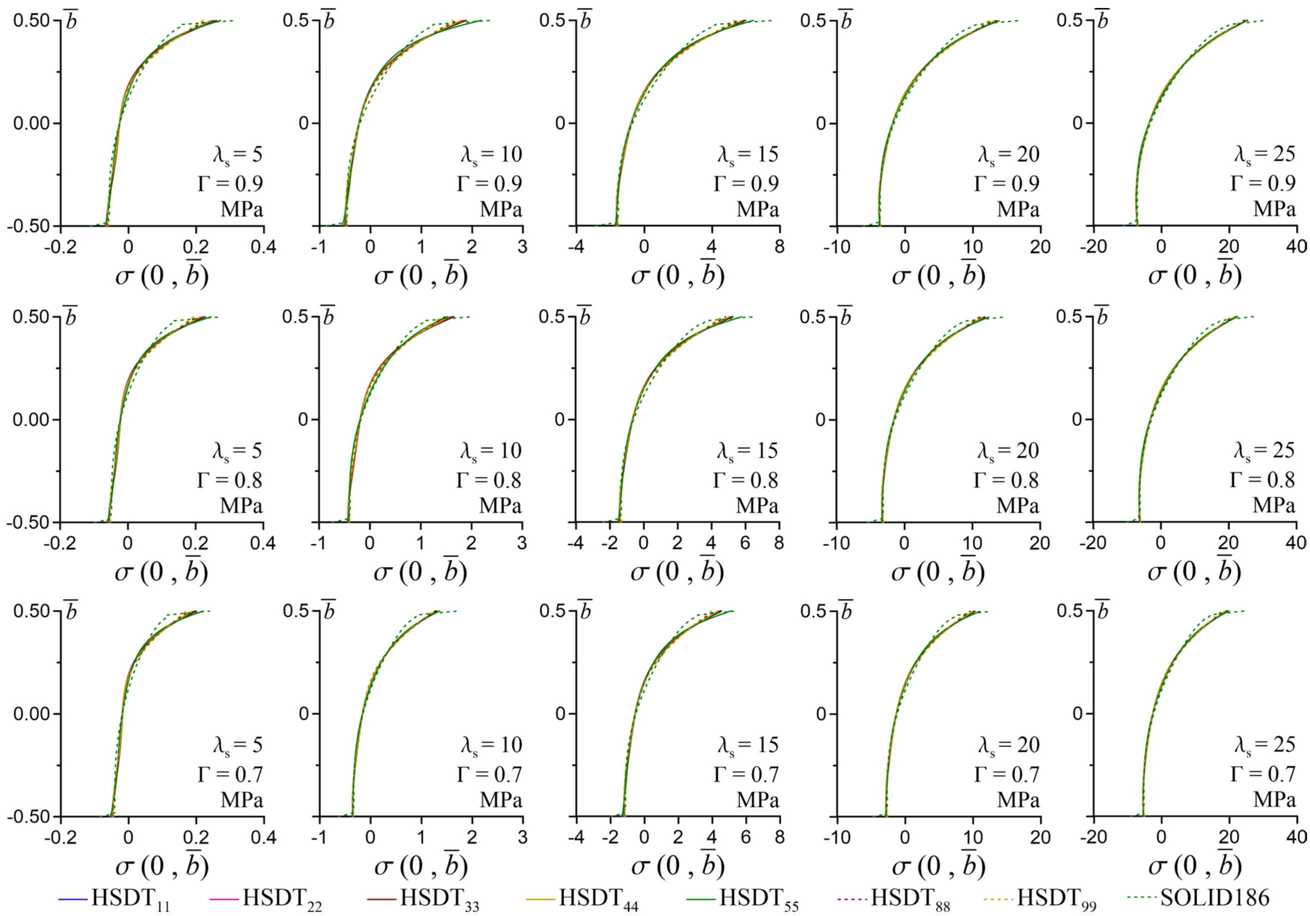

Fig. 17 Influence of Γ on the through-thickness $\sigma\left(0,\bar{b}\right)$

Table 7 Normal/shear stress components (MPa) of solid FEs for λ_E

			$\sigma(0,0.50)$			$\sigma(0,0.48)$			$\sigma(0.05,0.50)$			$\tau_{\max}\left(0,\bar{b}\right)$			$\tau_{\max}\left(0.05,\bar{b}\right)$		
Γ	λ_s	λ_E	5.43	3.45	1.81	5.43	3.45	1.81	5.43	3.45	1.81	5.43	3.45	1.81	5.43	3.45	1.81
1.0	5		0.37	0.34	0.30	0.17	0.16	0.14	0.15	0.14	0.12	0.106	0.098	0.087	0.009	0.009	0.008
	10		2.77	2.57	2.25	1.40	1.28	1.12	1.23	1.12	0.95	0.778	0.724	0.639	0.032	0.032	0.031
	15		8.96	8.28	7.29	4.77	4.37	3.84	4.14	3.77	3.22	2.399	2.232	1.972	0.073	0.071	0.070
0.9	5		0.32	0.29	0.26	0.15	0.14	0.12	0.14	0.13	0.11	0.084	0.078	0.069	0.009	0.008	0.008
	10		2.39	2.21	1.94	1.23	1.13	0.99	1.09	0.99	0.85	0.655	0.610	0.538	0.031	0.030	0.030
	15		7.73	7.15	6.29	4.19	3.84	3.37	3.68	3.35	2.86	2.033	1.893	1.673	0.069	0.067	0.066
0.8	5		0.28	0.26	0.23	0.13	0.12	0.11	0.12	0.11	0.09	0.078	0.073	0.064	0.008	0.008	0.008
	10		2.02	1.87	1.64	1.06	0.97	0.85	0.95	0.87	0.74	0.522	0.487	0.431	0.029	0.028	0.028
	15		6.56	6.06	5.33	3.65	3.34	2.94	3.22	2.93	2.51	1.680	1.564	1.383	0.064	0.062	0.061
0.7	5		0.24	0.22	0.19	0.11	0.10	0.09	0.10	0.10	0.08	0.069	0.064	0.057	0.008	0.008	0.007
	10		1.74	1.54	1.35	0.90	0.83	0.73	0.83	0.76	0.65	0.397	0.371	0.329	0.027	0.026	0.026
	15		5.42	5.02	4.41	3.14	2.88	2.53	2.81	2.55	2.18	1.334	1.244	1.100	0.058	0.057	0.057

respectively and compared to the stresses of solid FEs. Referring to the geometric features and loading in Sect. 3, the radius-to-thickness ratio is successively set to $\lambda_s = R_{\max}/h = 5,\ 10,\ 15$ for each ellipticity ratios $\Gamma = R_{\min}/R_{\max} = 1.0,\ 0.9,\ 0.8,\ 0.7$ ($R_{\max} = 3.0\text{m}$). Al, Cu and St are considered as the FGM constituents at the bottom of the section successively; while, the FGM constituent at the top is Al_2O_3 (Table 2). The ratios of the elasticity moduli of Al_2O_3–Al, Al_2O_3–Cu and Al_2O_3–St are $\lambda_E = 5.43$, 3.45 and 1.81, respectively. The power-law index is $p = 1$.

First, the normal/shear stress components of solid FEs are tabulated in Table 7 for each λ_E, λ_s and Γ. In each case of Γ and λ_s, as λ_E successively increases to 3.45 and 5.43, the both maximum stresses $\sigma(0, 0.50)$ and $\tau_{\max}\left(0, \bar{b}\right)$ become ~1.14 and ~1.22 times greater than the maximum stresses of $\lambda_E = 1.81$, respectively. The increase in λ_E influences $\sigma(0.05, 0.50)$ more than $\sigma(0, 0.50)$ since $\sigma(0.05, 0.50)$ becomes ~1.17 and ~1.29 times greater, respectively as λ_E increases. However, it influences $\tau_{\max}\left(0.05, \bar{b}\right)$ less than $\tau_{\max}\left(0, \bar{b}\right)$ since $\tau_{\max}\left(0.05, \bar{b}\right)$ becomes ~1.02 and ~1.05 times greater, respectively.

The increases in the normal/shear stresses through the clamped end and the increase in the normal stress through the top of section are given due to λ_E in Table 8. The increase in $\sigma\left(\bar{t}, 0.50\right)$ through the clamped end is denoted by the ratio $\beta_t^\sigma = \sigma(0, 0.50)/\sigma(0.05, 0.50)$. β_t^σ becomes greater as λ_E decreases except for the case $\Gamma = 0.7$ and $\lambda_s = 10$. In each case of λ_E, β_t^σ increases as Γ increases and/or λ_s decreases. The maximum and minimum β_t^σ are 2.51 ($\Gamma = 1.0$, $\lambda_s = 5$, $\lambda_E = 1.81$) and 1.93 ($\Gamma = 0.7$, $\lambda_s = 15$, $\lambda_E = 5.43$), respectively. The increase in $\sigma\left(0, \bar{b}\right)$ through the top of section is denoted by the ratio $\beta_b^\sigma = \sigma(0, 0.50)/\sigma(0, 0.48)$. β_b^σ increases as λ_E decreases except for the cases $\lambda_s = 10$ and $\Gamma = 0.7$, $\lambda_s = 5$ and $\Gamma = 0.8$, and $\lambda_s = 5$ and $\Gamma = 0.7$. In each case of λ_E, β_b^σ becomes greater as λ_s decreases. Besides, it has a tendency of increase as Γ increases. The maximum and minimum β_b^σ are 2.16 ($\Gamma = 0.7$, $\lambda_s = 5$, $\lambda_E = 5.43$) and 1.73 ($\Gamma = 0.7$, $\lambda_s = 15$, $\lambda_E = 5.43$), respectively. The increase in $\tau_{\max}\left(\bar{t}, \bar{b}\right)$ through the clamped end is denoted by the ratio $\beta_t^\tau = \tau_{\max}\left(0, \bar{b}\right) \Big/ \tau_{\max}\left(0.05, \bar{b}\right)$. β_t^τ becomes greater as Γ and/or λ_s and/or λ_E increase.

The through-thickness normal stresses $\sigma\left(0.05, \bar{b}\right)$ are illustrated as λ_E decreases via $HSDT_{33}$ and solid FEs in Fig. 18. The maximum normal stresses $\sigma_{\max}\left(0.05, \bar{b}\right)$ of $HSDT_{33}$ are tabulated for each Γ, λ_s and λ_E in Table 9 and the percent differences with respect to the solid FEs (Table 7) are given. In each case, the percent differences for $\lambda_E = 3.45$ are greater than $\lambda_E = 5.43$ and 1.81. The minimum percent difference is obtained in the case of $\Gamma = 1$, $\lambda_s = 15$ and $\lambda_E = 5.43$ as 0.65%. It becomes 0.95% for $\Gamma = 1$, $\lambda_s = 15$ and $\lambda_E = 3.45$. Besides, the decrease in Γ and/or λ_s increases the percent difference. It increases to 1.45% as λ_s decreases to 5 ($\Gamma = 1$). The inclusion of decrease in Γ results it to be 4.39% ($\Gamma = 0.7$).

The through-thickness shear stresses $\tau\left(0.05, \bar{b}\right)$ are illustrated as λ_E decreases via BDHSDFs and solid FEs in Fig. 19. Successively in the cases of $\lambda_s = 5$, 10 and 15, a better convergence is obtained via $HSDT_{55}$, $HSDT_{33}$ and $HSDT_{33}$ for $\Gamma = 1.0$, $HSDT_{22}$, $HSDT_{99}$ and $HSDT_{99}$ for $\Gamma = 0.9$, $HSDT_{55}$, $HSDT_{88}$ and $HSDT_{55}$ for $\Gamma = 0.8$, and $HSDT_{55}$, $HSDT_{55}$ and $HSDT_{55}$ for $\Gamma = 0.7$. Thus, $\tau\left(0.05, \bar{b}\right)$ is given in Fig. 19 for the abovementioned BDHSDFs. The maximum $\tau_{\max}\left(0.05, \bar{b}\right)$ of BDHSDFs are tabulated in Table 10 and the percent differences with respect to the solid FEs (Table 7) are given. The minimum percent difference is obtained for $\lambda_E = 3.45$ as 0.18% ($\Gamma = 0.8$, $\lambda_s = 10$). As Γ decreases to 0.7 and/or λ_s decreases to 5, a decrease in λ_E results an increase in the percent differences. However, as Γ and λ_s increases, it is quite the opposite. In the case of $\Gamma = 1$, the maximum percent difference is obtained for $\lambda_s = 10$ and

Table 8 Increase in stresses of solid FEs as λ_E increases. $\beta_b^\sigma = \sigma(0, 0.50)/\sigma(0, 0.48)$, $\beta_t^\sigma = \sigma(0, 0.50)/\sigma(0.05, 0.50)$ and $\beta_t^\tau = \tau_{\max}(0, \bar{b}) \Big/ \tau_{\max}(0.05, \bar{b})$

			β_b^σ			β_t^σ			β_t^τ		
Γ	λ_s	λ_E	5.43	3.45	1.81	5.43	3.45	1.81	5.43	3.45	1.81
1.0	5		2.13	2.15	2.16	2.40	2.45	2.51	11.94	11.40	10.31
	10		1.98	2.00	2.01	2.26	2.30	2.36	23.99	22.83	20.40
	15		1.88	1.89	1.90	2.16	2.20	2.26	32.95	31.35	28.02
0.9	5		2.05	2.07	2.07	2.30	2.35	2.41	9.83	9.40	8.57
	10		1.94	1.96	1.96	2.19	2.23	2.29	21.34	20.31	18.23
	15		1.84	1.86	1.86	2.10	2.13	2.20	29.61	28.17	25.28
0.8	5		2.10	2.06	2.06	2.30	2.34	2.40	9.58	9.10	8.31
	10		1.91	1.93	1.93	2.12	2.15	2.22	18.23	17.37	15.63
	15		1.80	1.81	1.82	2.04	2.07	2.13	26.40	25.24	22.63
0.7	5		2.16	2.12	2.13	2.28	2.32	2.39	8.98	8.54	7.82
	10		1.93	1.85	1.85	2.09	2.04	2.10	14.86	14.18	12.82
	15		1.73	1.74	1.74	1.93	1.96	2.02	22.82	21.69	19.45

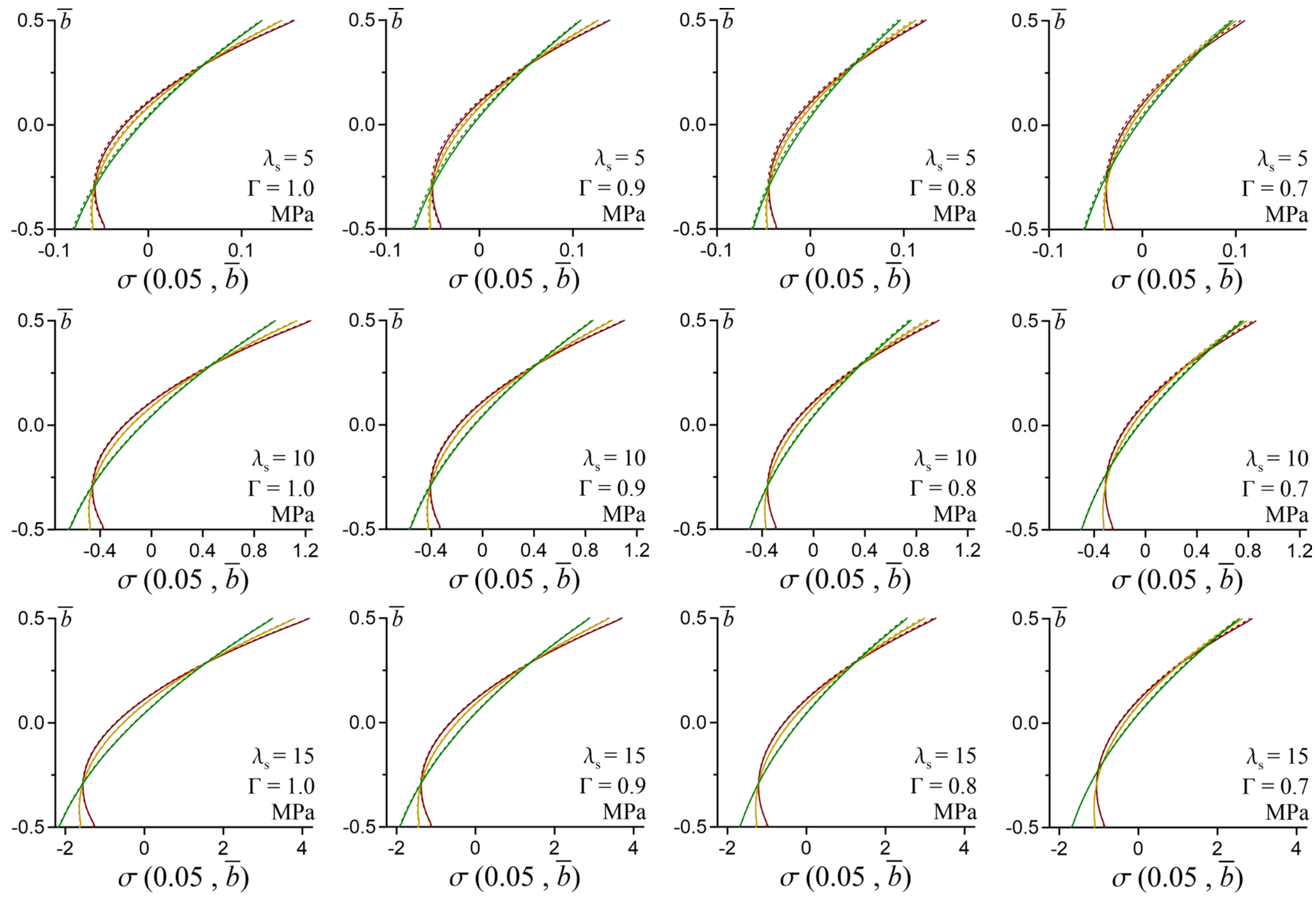

Fig. 18 $\sigma\left(0.05, \overline{b}\right)$ due to $\lambda_E = 5.43$, 3.45 and 1.81 (Red, yellow and green lines, respectively). Continuous and dashed lines are HSDT$_{33}$ and solid FEs, respectively

Table 9 $\sigma_{\max}\left(0.05, \overline{b}\right)$ of HSDT$_{33}$. Diff.% $= 100\times\left[\left(\mathrm{HSDT}_{33}/\mathrm{SOLID186}\right) - 1\right]$

		Γ	1.0			0.9			0.8			0.7		
	λ_E	λ_s	5	10	15	5	10	15	5	10	15	5	10	15
MPa	5.43		0.16	1.24	4.17	0.14	1.10	3.71	0.12	0.98	3.27	0.11	0.86	2.88
	3.45		0.14	1.13	3.81	0.13	1.01	3.38	0.11	0.89	2.99	0.10	0.78	2.62
	1.81		0.12	0.96	3.24	0.11	0.86	2.88	0.10	0.76	2.55	0.10	0.76	2.55
Diff.%	5.43		1.08	0.97	0.65	1.33	1.12	0.70	2.75	2.36	1.73	4.11	3.03	2.43
	3.45		1.45	1.28	0.95	1.69	1.43	1.00	2.87	2.51	1.91	4.39	3.51	2.75
	1.81		1.31	1.00	0.66	1.55	1.12	0.69	2.77	2.19	1.60	4.35	3.18	2.45

$\lambda_E = 5.43$ as 5.21%. Although the percent difference tends to increase as Γ and λ_E increases in the cases of $\lambda_s = 10$ and 15, it is quite the opposite for $\lambda_s = 5$. The maximum percent differences are obtained in the case of $\lambda_s = 5$ for $\Gamma = 0.9$, 0.8 and 0.7. However, it is not the case for $\Gamma = 1.0$.

3.2.5 Power-law index

The influence of increase in the power-law index p on the maximum normal/shear stress components of TFG exact curved beams is investigated via solid FEs and BDHSDFs in this section. $\theta_{\mathrm{UN}} = 0.0002\theta$ and 0.009θ are used to determine the normal and shear stresses of BDHSDFs, respectively, referred to the Sects. 3.2.1–3.2.2. The loading and geometric features which results the maximum/minimum percent differences of BDHSDFs compared to the solid FEs in the Sect. 3.2.4 are the scope of this section. Thus, the ellipticity ratios $\Gamma = R_{\min}/R_{\max} = 1.0$ and 0.7 ($R_{\max} = 3.0$m) and the radius-to-thickness ratios $\lambda_s = R_{\max}/h = 5$ and 15 are taken into consideration. While keeping the top of TFG sections

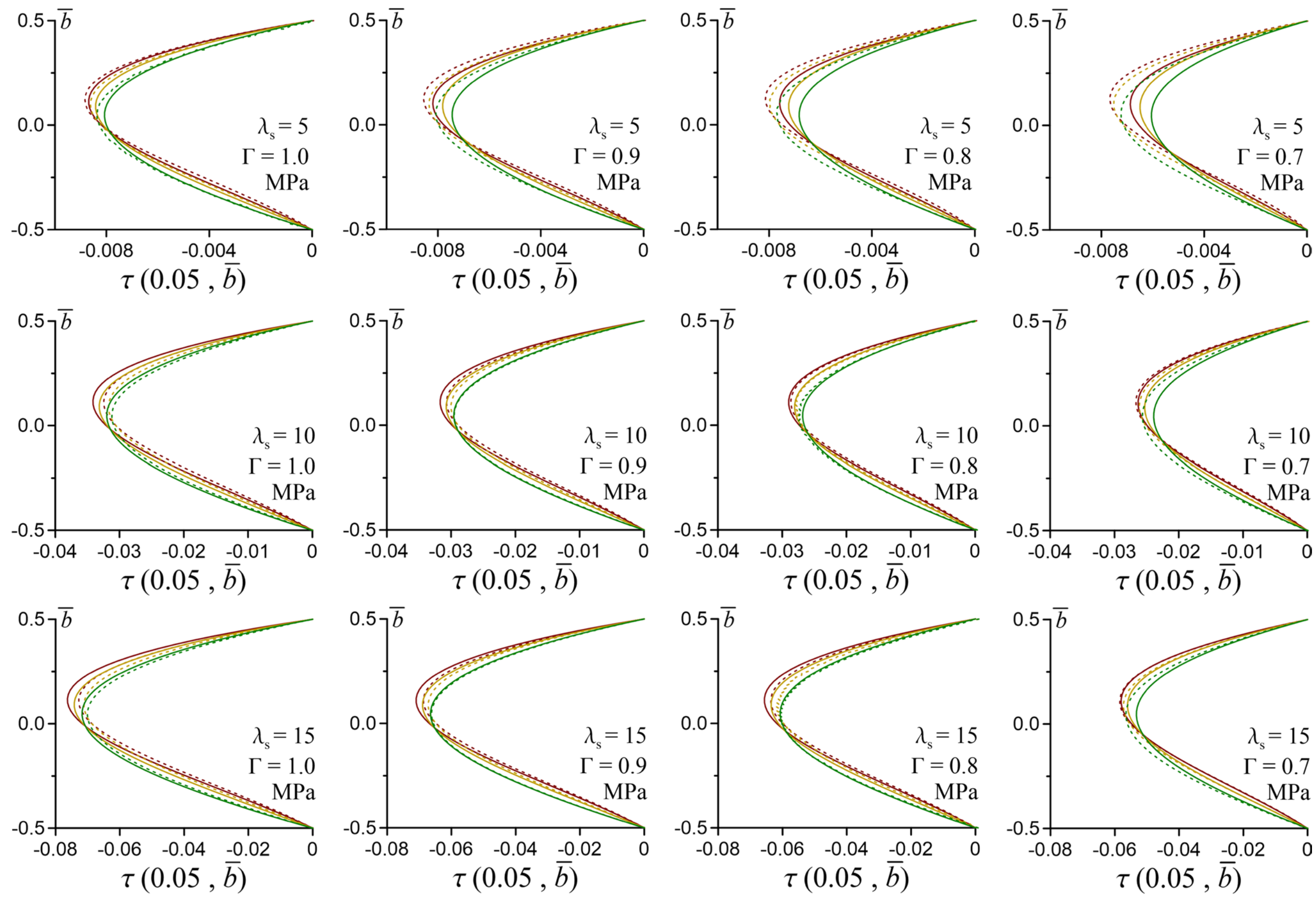

Fig. 19 $\tau\left(0.05, \bar{b}\right)$ due to $\lambda_E = 5.43$, 3.45 and 1.81 (Red, yellow and green lines, respectively). Continuous and dashed lines are BDHSDFs and solid FEs, respectively

Table 10 $\left|\tau_{\max}\left(0.05, \bar{b}\right)\right|$ of BDHSDFs. Diff.% $= 100 \times \left[(\text{BDHSDFs}/\text{SOLID186}) - 1\right]$

	Γ		1.0			0.9			0.8			0.7		
	λ_E	λ_s	5	10	15	5	10	15	5	10	15	5	10	15
MPa	5.43		0.009	0.034	0.076	0.008	0.032	0.071	0.008	0.029	0.066	0.007	0.026	0.058
	3.45		0.008	0.033	0.074	0.008	0.031	0.069	0.007	0.028	0.064	0.006	0.025	0.056
	1.81		0.008	0.032	0.072	0.007	0.030	0.066	0.007	0.027	0.061	0.006	0.024	0.053
Diff.%	5.43		−1.74	5.21	4.84	−4.17	3.24	3.30	−6.79	1.19	3.16	−10.31	−1.26	−0.70
	3.45		−2.34	4.53	4.24	−6.38	2.47	2.62	−9.42	0.18	2.52	−13.59	−3.19	−2.23
	1.81		−3.50	2.53	2.44	−7.85	0.19	0.48	−11.41	−2.61	−0.65	−16.42	−6.89	−5.78

as Al_2O_3, the bottom is successively set to Al, Cu and St. The elasticity moduli ratios of Al_2O_3 to Al, Cu and St are $\lambda_E = 5.43$, 3.45 and 1.81, respectively. The power-law index p is set to 1, 2 and 3 successively for each abovementioned Γ, λ_s and λ_E.

The increase in the normal/shear stress components through the clamped end of solid FEs related to an increase in p is tabulated in Tables 11 and 12 for each Γ, λ_s and λ_E. The increase in the normal stress through the clamped end $\beta_t^\sigma = \sigma(0, 0.50)/\sigma(0.05, 0.50)$ becomes greater as Γ increases and/or λ_s decreases (Table 11). Besides, a decrease in λ_E results an increase in β_t^σ. In the case of $\lambda_s = 5$, β_t^σ becomes greater as p increases. However, p is not directly proportional to β_t^σ for $\lambda_s = 15$. In the case of $\Gamma = 1.0$ and $\lambda_s = 15$, the minimum β_t^σ is obtained for $p = 2$. The maximum β_t^σ is obtained as 2.79 in the case of $\Gamma = 1.0$, $\lambda_s = 5$, $\lambda_E = 1.81$ and $p = 3$.

The increase in the shear stress through the clamped end $\beta_t^\tau = \tau_{\max}(0,\overline{b}) \big/ \tau_{\max}(0.05,\overline{b})$ becomes greater as Γ and/or λ_s and/or λ_E increase (Table 12). In the case of $\lambda_s = 15$, β_t^τ decreases as p increases. However, as λ_s decreases to 5, the maximum β_t^τ is obtained in the cases $p = 3$ and 2 for $\Gamma = 1.0$ and 0.7, respectively. While $\beta_t^\tau = 8.73$ for $\Gamma = 0.7$, $\lambda_s = 5$, $\lambda_E = 3.45$ and $p = 3$, it increases to 32.95 as p decreases to 1 and Γ, λ_s and λ_E increase to 1.0, 15 and 5.43, respectively.

The maximum percent difference of $\sigma_{\max}\left(0.05,\overline{b}\right)$ is obtained for $\Gamma = 0.7$ and $\lambda_s = 5$ while performing the convergence of HSDT$_{33}$ compared to the solid FEs in Table 9. Thus, $\sigma\left(0.05,\overline{b}\right)$ of HSDT$_{33}$ and solid FEs are illustrated for these geometric features in Fig. 20 as p increases. In the cases of $p = 2$ and 3, the percent differences of $\sigma_{\max}\left(0.05,\overline{b}\right)$ compared to solid FEs (Table 11) becomes 4.22% (0.111MPa) and 4.42% (0.118MPa), respectively, for $\lambda_E = 3.45$, and 4.26% (0.090MPa) and 4.45% (0.093MPa), respectively, for $\lambda_E = 1.81$. Although the

Table 11 The increase in normal stress $\beta_t^\sigma = \sigma(0, 0.50)/\,\sigma(0.05, 0.50)$ for solid FEs (MPa)

			$\sigma(0, 0.50)$						$\sigma(0.05, 0.50)$						$\beta_t^\sigma\,\beta_t^\sigma$					
		λ_E	3.45			1.81			3.45			1.81			3.45			1.81		
Γ	λ_s	p	1	2	3	1	2	3	1	2	3	1	2	3	1	2	3	1	2	3
1.0	15		8.28	8.82	9.92	7.29	7.43	8.20	3.77	4.20	4.44	3.22	3.40	3.52	2.20	2.10	2.23	2.26	2.19	2.33
	5		0.34	0.40	0.45	0.30	0.34	0.37	0.14	0.16	0.17	0.12	0.13	0.13	2.45	2.56	2.70	2.51	2.64	2.79
0.7	15		5.02	5.73	6.08	2.55	2.84	3.52	4.41	4.83	5.02	2.51	2.30	2.38	1.96	2.02	1.73	2.02	2.10	2.11
	5		0.22	0.27	0.30	0.19	0.23	0.25	0.10	0.11	0.11	0.08	0.09	0.09	2.32	2.54	2.66	2.39	2.64	2.76

Table 12 The increase in shear stress $\beta_t^\tau = \tau_{\max}(0,\overline{b}) \big/ \tau_{\max}(0.05,\overline{b})$ for solid FEs (MPa)

			$\tau_{\max}\left(0,\overline{b}\right)$						$\tau_{\max}\left(0.05,\overline{b}\right)$						$\beta_t^\tau\,\beta_t^\tau$					
		λ_E	5.43			3.45			5.43			3.45			5.43			3.45		
Γ	λ_s	p	1	2	3	1	2	3	1	2	3	1	2	3	1	2	3	1	2	3
1.0	15		2.40	1.95	1.89	2.23	1.77	1.70	0.07	0.07	0.07	0.07	0.07	0.07	32.95	27.21	26.93	31.35	25.21	24.59
	5		0.11	0.11	0.12	0.10	0.10	0.11	0.01	0.01	0.01	0.01	0.01	0.01	11.94	11.94	13.97	11.40	11.20	13.08
0.7	15		1.33	1.30	1.09	1.24	1.18	1.00	0.06	0.06	0.06	0.06	0.06	0.06	22.82	22.56	19.07	21.69	20.82	17.68
	5		0.07	0.08	0.07	0.06	0.07	0.06	0.01	0.01	0.01	0.01	0.01	0.01	8.98	10.00	9.50	8.54	9.31	8.73

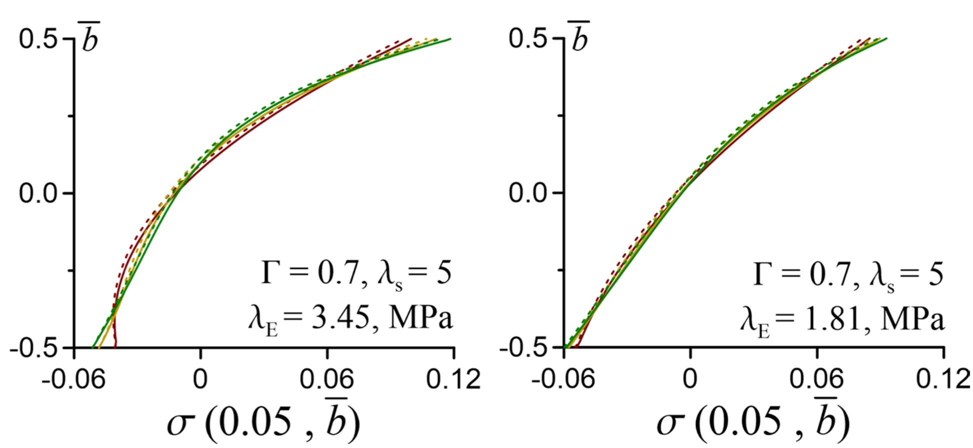

Fig. 20 $\sigma\left(0.05,\overline{b}\right)$ due to $p = 1$, 2 and 3 (Red, yellow and green lines, respectively). Continuous and dashed lines are HSDT$_{33}$ and solid FEs, respectively

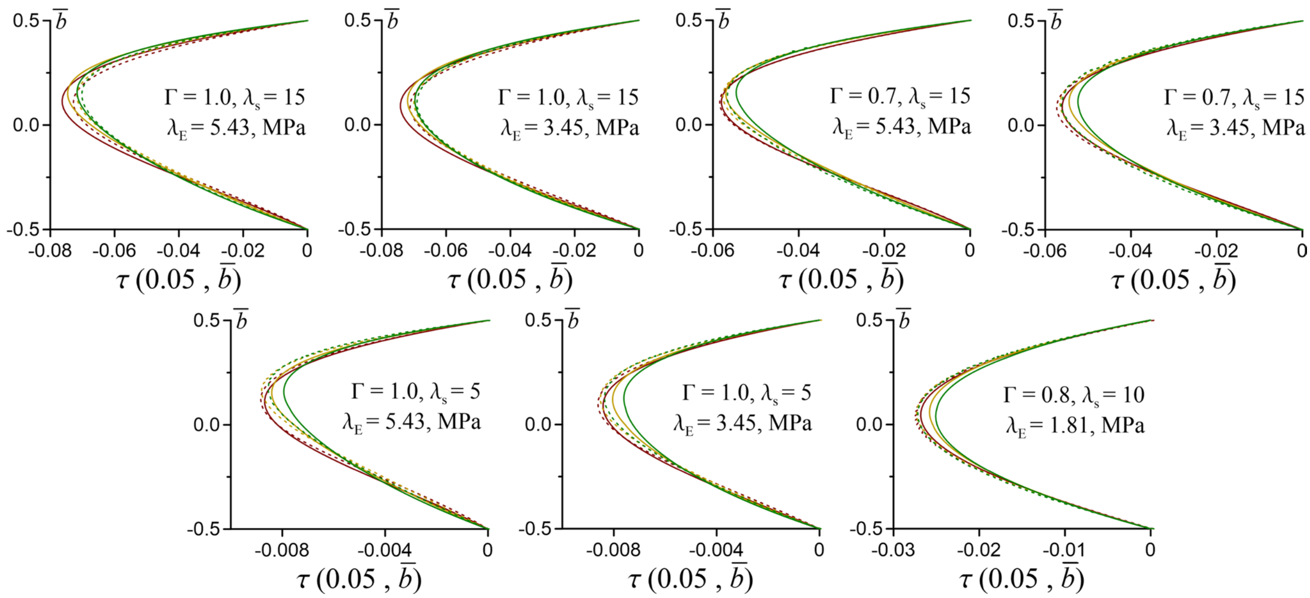

Fig. 21 $\tau\left(0.05,\overline{b}\right)$ due to p = 1, 2 and 3 (Red, yellow and green lines, respectively). Continuous and dashed lines are BDHSDFs and solid FEs, respectively

Table 13 $\left|\tau_{\max}\left(0.05,\overline{b}\right)\right|$ of BDHSDFs. Diff.% = 100× [(BDHSDFs/ SOLID186) − 1]

		Γ	1.0				0.7		0.8
		λ_s	15		5		15		10
	p	λ_E	5.43	3.45	5.43	3.45	5.43	3.45	1.81
MPa	1		0.076	0.074	0.009	0.008	0.058	0.056	0.027
	2		0.075	0.072	0.008	0.008	0.057	0.054	0.026
	3		0.072	0.070	0.008	0.008	0.055	0.052	0.025
Diff.%	1		4.84	4.24	−1.74	−2.34	−0.70	−2.23	−2.61
	2		4.02	2.84	−4.49	−5.59	−1.22	−3.72	−5.50
	3		2.14	0.91	−7.56	−9.00	−4.31	−7.18	−7.67

maximum difference is obtained as 4.39% for $\lambda_E = 3.45$ in the case of $p = 1$, it increases to 4.45% as p increases to 3.

The through-thickness shear stresses $\tau\left(0.05,\overline{b}\right)$ of BDHSDFs and solid FEs are illustrated in Fig. 21 as p increases. The range of the geometric features and FGM constituents is specified by means of the conclusions in Sect. 3.2.4 which have less than 5.0% percent difference compared to solid FEs (Table 10, $p = 1$). $\tau\left(0.05,\overline{b}\right)$ is determined via BDHSDFs given in Sect. 3.2.4 related to Γ and λ_s, and the percent difference of $\tau_{\max}\left(0.05,\overline{b}\right)$ compared to solid FEs are tabulated in Table 13 as p increases. The absolute $\left|\tau_{\max}\left(0.05,\overline{b}\right)\right|$ of BDHSDFs are greater than solid FEs in the case of $\Gamma = 1.0$ and $\lambda_s = 15$. The percent difference tends to increase by the decrease in Γ as p increases. A decrease in λ_s increases the percent differences except the case $\Gamma = 1.0$, $\lambda_E = 5.43$ and 3.45 and $p = 1$. Although the percent difference tends to increase as λ_E decreases, it is quite the opposite for $\Gamma = 1.0$ and $\lambda_s = 15$. In the cases of $\Gamma = 0.7$ or $\lambda_s = 5$, an increase in p results an increase in the percent differences. However, it is quite the opposite in the case of $\Gamma = 1.0$ and $\lambda_s = 15$.

3.2.6 Bi-directional Higher-order Shear Deformation

This section presents the efficiency of specifying transverse HSDF on the determination of accurate normal/shear stress components for TFG spatial curved beams via BDHSDFs. Besides, the influences of the ratio of elasticity moduli of FGM constituents λ_E and power-law index p on the normal/shear stress components are investigated. The centerline radius on plane, height, the radius-to-thickness ratio

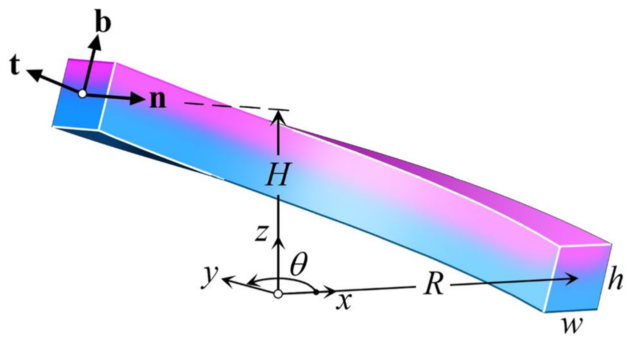

Fig. 22 TFG spatial curved beam

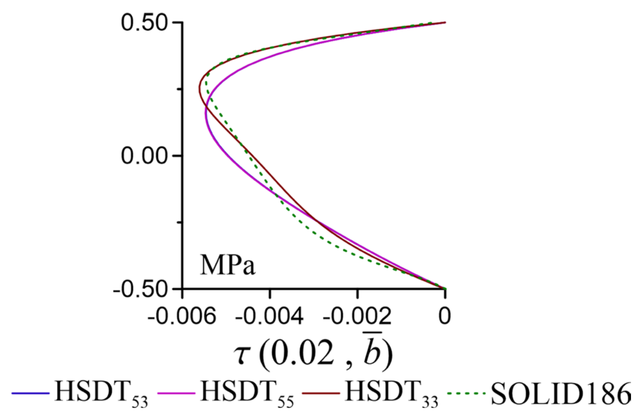

Fig. 24 $\tau\left(0.02,\bar{b}\right)$ of $HSDT_{33}$, $HSDT_{53}$, and $HSDT_{55}$

and the central arch length angle of spatial curved beam are kept constant as $R = 3.0\,\mathrm{m}$, $H = 1.5\,\mathrm{m}$, $\lambda_s = 5$ and $\theta = 90°$, respectively (Fig. 22). Both ends of the spatial curved square beam are clamped and it is under the influence of a 0.5kN/m uniformly distributed load in the direction of -*z* axis. The bottom of the section is successively set to Al, Cu and St for each $p = 1$, 2 and 3 while the top is Al_2O_3 (Table 2). λ_E are 5.43, 3.45 and 1.81 for Al_2O_3–Al, Al_2O_3–Cu and Al_2O_3–St, respectively.

First, $\sigma\left(0,\bar{b}\right)$, $\tau\left(0,\bar{b}\right)$ and $\tau\left(0.02,\bar{b}\right)$ of $HSDT_{31}$ – $HSDT_{39}$ are obtained via $\theta_{UN} = 0.002\theta$, 0.009θ and 0.009θ, respectively, for $\lambda_E = 5.43$ and $p = 1$ (Fig. 23). Besides, $\tau\left(0.02,\bar{b}\right)$ of $HSDT_{33}$, $HSDT_{53}$, $HSDT_{55}$ are illustrated graphically in Fig. 24 $\left(\theta_{UN} = 0.009\theta\right)$. Since there are stress-free conditions for BDHSDFs different from solid FEs in the case of $\tau\left(0,\bar{b}\right)$, the percent differences of $\sigma_{\max}\left(0,\bar{b}\right)$ and $\tau_{\max}\left(0.02,\bar{b}\right)$ are tabulated in Table 14. The minimum percent difference of $\sigma_{\max}\left(0,\bar{b}\right)$ compared to the solid FEs is obtained for $HSDT_{33}$ as -1.41%. The percent differences of $\tau_{\max}\left(0.02,\bar{b}\right)$ for $HSDT_{33}$, $HSDT_{53}$ and $HSDT_{55}$ compared to solid FEs are 2.75% (−5.61kPa), 0.03% (−5.46kPa) and 0.23% (−5.47kPa), respectively (Fig. 24). Despite its percent difference, $HSDT_{33}$ is preferred due to the variation of $\tau\left(0.02,\bar{b}\right)$ through the thickness.

Since the precision can be increased more via θ_{UN}, the normal stress $\sigma\left(0,\bar{b}\right)$ of $HSDT_{33}$ is compared to solid FEs for various θ_{UN} as λ_E and/or p increase in Fig. 25. $\sigma_{\max}\left(0,\bar{b}\right)$ of solid FEs for $p = 1$, 2 and 3 are 0.096MPa, 0.118MPa and 0.104MPa, respectively, in the case of $\lambda_E = 5.43$, 0.089MPa, 0.106MPa and 0.091MPa, respectively, in the case of $\lambda_E = 3.45$, and 0.078MPa, 0.087MPa and 0.073MPa, respectively, in the case of $\lambda_E = 1.81$. The greatest normal stresses $\sigma_{\max}\left(0,\bar{b}\right)$ of solid FEs are obtained for $p = 2$ compared to $p = 1$ and 3. Besides, $\sigma_{\max}\left(0,\bar{b}\right)$ increases as λ_E increases. The minimum percent differences of $HSDT_{33}$ compared to $\sigma_{\max}\left(0,\bar{b}\right)$ of solid FEs for $p = 1$, 2 and 3 are -1.41% (0.094MPa, $\theta_{UN} = 0.002\theta$), 0.15% (1.118MPa, $\theta_{UN} = 0.001\theta$) and -0.27% (0.104MPa, $\theta_{UN} = 0.004\theta$), respectively, in the case of $\lambda_E = 5.43$. In the case of $\lambda_E = 3.45$, they become -2.78% (0.086MPa, $\theta_{UN} = 0.002\theta$),

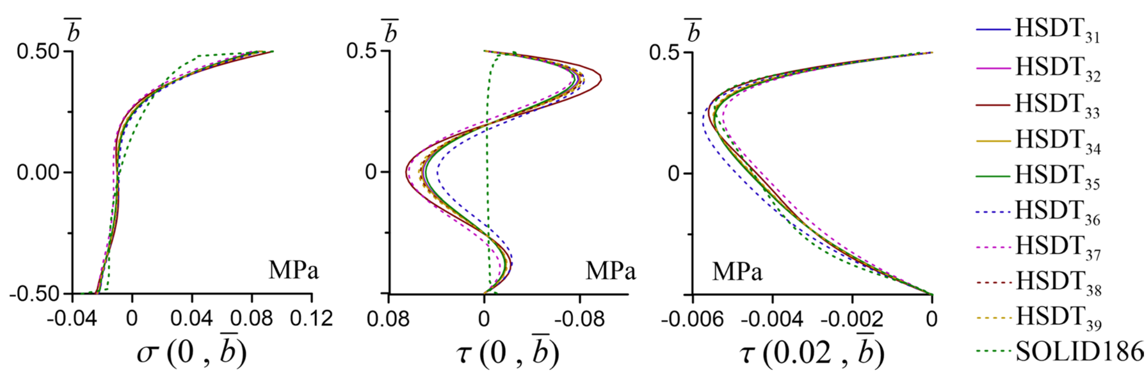

Fig. 23 Through-thickness stresses of $HSDT_{3j}$, $j = 1$–9

Table 14 $\sigma_{\max}\left(0,\bar{b}\right)$ in MPa and $\left|\tau_{\max}\left(0.02,\bar{b}\right)\right|$ in kPa of $\mathrm{HSDT}_{31}-\mathrm{HSDT}_{39}$. Diff.% $=100\times\left[(\mathrm{BDHSDFs}/\mathrm{SOLID186})-1\right]$

	HSDT_{ij}									
$ij=$	31	32	33	34	35	36	37	38	39	SOLID186
$\sigma_{\max}\left(0,\bar{b}\right)$	0.085	0.085	0.094	0.085	0.083	0.087	0.081	0.086	0.087	0.096
Diff.%	− 11.27	− 10.93	− 1.41	− 10.58	− 12.79	− 9.16	− 15.70	− 9.81	− 8.90	
$\left\|\tau_{\max}\left(0.02,\bar{b}\right)\right\|$	5.47	5.47	5.61	5.48	5.46	5.75	5.24	5.48	5.49	5.46
Diff.%	0.23	0.27	2.75	0.32	0.02	5.39	− 3.90	0.45	0.65	

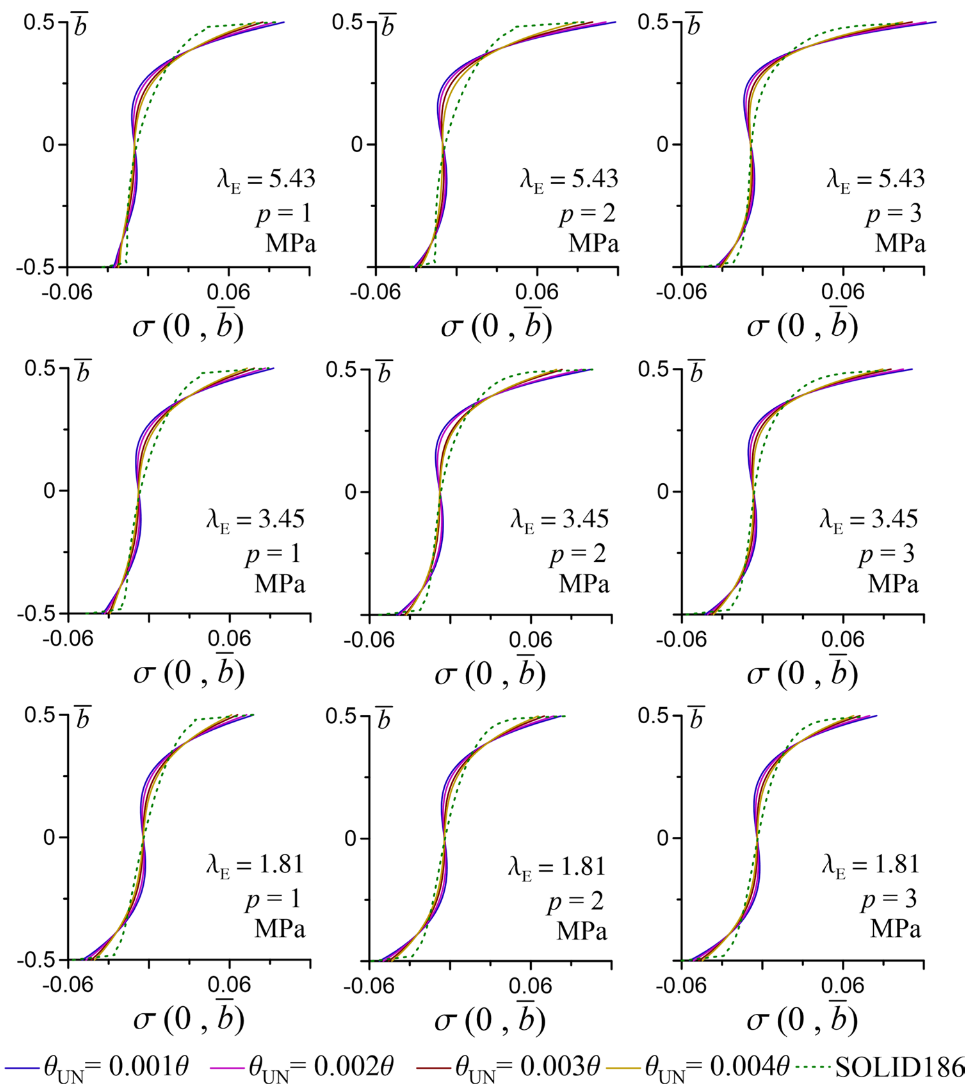

Fig. 25 $\sigma\left(0,\bar{b}\right)$ of HSDT_{33} for various θ_{UN} as λ_E and/or p increase

− 1.49% (0.104MPa, $\theta_{UN}=0.001\theta$) and − 2.42% (0.089MPa, $\theta_{UN}=0.004\theta$), respectively. Finally in the case of $\lambda_E=1.81$, they become 0.14% (0.078MPa, $\theta_{UN}=0.001\theta$), − 5.47% (0.082MPa, $\theta_{UN}=0.001\theta$) and − 0.62% (0.072MPa, $\theta_{UN}=0.003\theta$), respectively.

The through-thickness shear stresses $\tau\left(0.02,\bar{b}\right)$ of HSDT_{33} are illustrated for $\theta_{UN}=0.009\theta$ in Fig. 26 compared to the solid FEs as λ_E and/or p increase. $\tau_{\max}\left(0.02,\bar{b}\right)$ of solid FEs for $p=1$, 2 and 3 are − 5.46kPa, − 5.83kPa and − 5.88kPa, respectively, in the case of $\lambda_E=5.43$, − 5.17kPa,

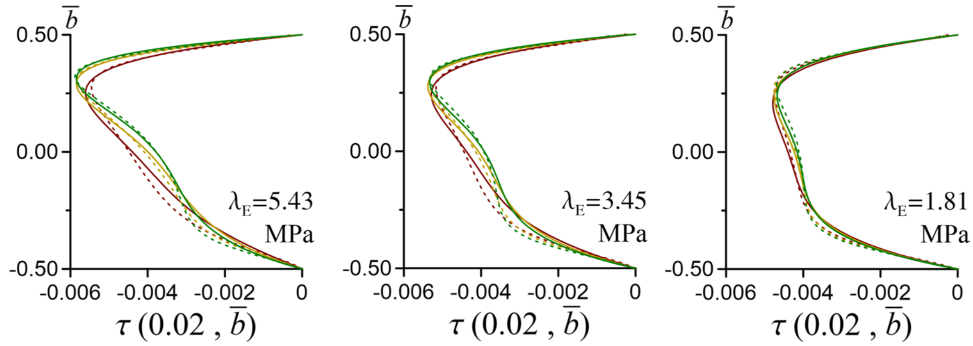

Fig. 26 $\tau\left(0.02, \overline{b}\right)$ due to $p = 1$, 2 and 3 (Red, yellow and green lines, respectively). Continuous and dashed lines are HSDT$_{33}$ and solid FEs, respectively

5.35kPa and -5.33kPa, respectively, in the case of $\lambda_E = 3.45$, and -4.74kPa, -4.76kPa and -4.70kPa, respectively, in the case of $\lambda_E = 1.81$. Similar to $\sigma\left(0, \overline{b}\right)$, the increase in λ_E increases the absolute $\left|\tau_{\max}\left(0.02, \overline{b}\right)\right|$. The minimum percent differences of HSDT$_{33}$ compared to $\tau_{\max}\left(0.02, \overline{b}\right)$ of solid FEs for $p = 1$, 2 and 3 are 2.75% (-5.61kPa), 0.29% (-5.85kPa) and -0.62% (-5.84kPa), respectively, in the case of $\lambda_E = 5.43$. In the case of $\lambda_E = 3.45$, they become 2.33% (-5.29kPa), 0.54% (-5.38kPa) and 0.05% (-5.33kPa), respectively. Finally, in the case of $\lambda_E = 1.81$, they become 0.94% (-4.79kPa), -0.13% (-4.75kPa) and -0.42% (-4.68kPa), respectively.

The displacements $u_t\left(\overline{t}\right)$ and $u_b\left(\overline{t}\right)$ at the normalized tangential coordinate $\overline{t} = 0.5$ of the TFG space curved beam having $\theta_{UN} = 0.002\theta$, $\lambda_E = 5.43$ and $p = 1$ are illustrated for HSDT$_{3j}$ and HSDT$_{5j}$ ($j = 1 - 9$) in Fig. 27. The implementation of transverse HSDFs influences the displacements more in the case of HSDT$_{5j}$. The absolute percent differences of maximum displacement with respect to the minimum displacement are 2.55% for $u_t(0.5)$ and 2.53% for $u_b(0.5)$ in the case of HSDT$_{3j}$, and 6.37% for $u_t(0.5)$ and 6.79% for $u_b(0.5)$ in the case of HSDT$_{5j}$. The displacements $u_b(0.5)$ of HSDT$_{56}$ and HSDT$_{57}$ converge more to the displacement $u_b(0.5) = 5.62 \times 10^{-7}$m of solid FEs whereas both percent differences with respect to the solid FEs are -0.25%. Thus, the influences of λ_E and p on the displacements $u_t(0.5)$ and $u_b(0.5)$ are also illustrated for HSDT$_{56}$ in Fig. 27. While keeping λ_E constant, as p increases from 1 to 3, both displacements become 1.29 and 1.44 times greater for $\lambda_E = 5.43$, 1.19 and 1.28 times greater for $\lambda_E = 3.45$, and 1.08 and 1.11 times greater for $\lambda_E = 1.81$. While keeping p constant, as λ_E increases from 1.81 to 5.43, both displacements become 1.29 and 1.48 times greater for $p = 1$, 1.42 and 1.77 times greater for $p = 2$, and 1.48 and 1.91 times greater for $p = 3$.

4 Conclusions

The capabilities of the proposed bi-directional higher-order shear deformation functions (BDHSDFs) in predicting the normal/shear stresses of transversely functionally graded (TFG) exact curved and spatial curved beams are presented via mixed FEM. The precision of BDHSDFs is assessed with respect to the stresses of solid FEs for various ellipticity ratios, radius-to-thickness ratios, ratios of elasticity moduli of FG material constituents and power-law indexes. Satisfactory results are obtained with lesser degree of

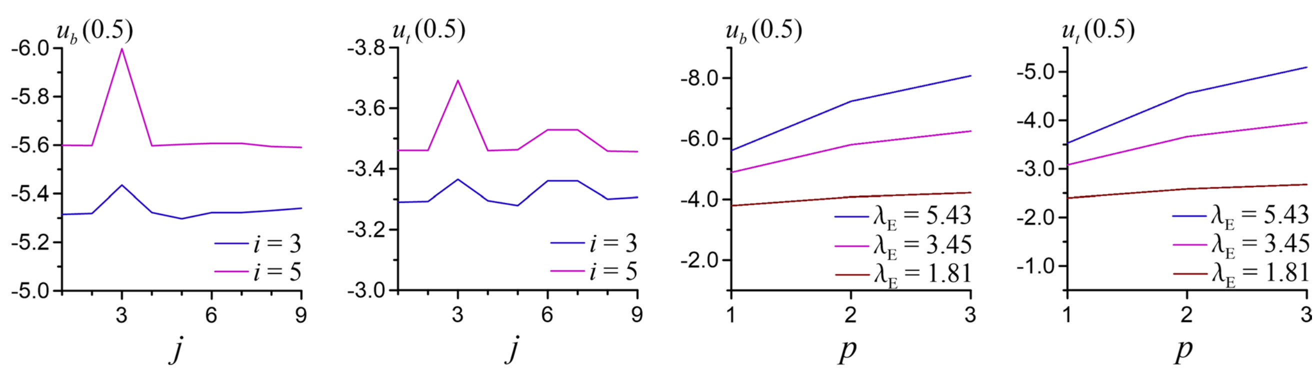

Fig. 27 $u_t(0.5)$ and $u_b(0.5)$ for various HSDT$_{ij}$ and the influences of λ_E and p on the displacements of the TFG space curved beam (the displacements are given in $\mathrm{m} \times 10^{-7}$)

freedoms compared to solid FEs. Besides, the precision can be increased more via the proposed accuracy elements or specifying transverse HSDFs. Another aim of this study is to present the influences of geometric features and material configurations on the stresses of TFG exact curved and spatial curved beams. The numerical results reveal that:

Convergence: The maximum influence of accuracy elements on the maximum normal stress at the clamped end is obtained for $HSDT_{55}$. The maximum normal stress at the clamped end converges to solid FEs more as the radius-to-thickness ratio decreases. Similarly, within the range of St. Venant principle, the maximum normal stress on the cross section at the normalized tangential coordinate $\bar{t} = t/S = 0.05$, where S is the total axial arc length, converges to solid FEs as the radius-to-thickness and/or ellipticity ratios decrease. The maximum percent difference of it compared to solid FEs in the case of $HSDT_{33}$ is obtained as 4.45%. At the same normalized tangential coordinate, the convergence of the maximum shear stress to solid FEs is satisfactory independent from the accuracy elements. As the ellipticity ratio decreases, the shear stress on the axis tends to converge to solid FEs, opposite rule exists when the radius-to-thickness ratio is equal to 5. An increase in the ratios of the elasticity moduli of functionally graded material constituents increases the percent difference of the maximum shear stress compared to solid FEs as the ellipticity and the radius-to-thickness ratio increases. The influences of accuracy elements or BDHSDFs on the results increase through the clamped end.

The Normal Stress: The rate of increase in the normal stress through the thickness at the clamped end becomes greater as the radius-to-thickness ratio decreases. Besides, the influence of the radius-to-thickness ratio on the decrease in the normal stress at the top of the clamped end becomes greater as it decreases. The increase in the ratios of the elasticity moduli of functionally graded material constituents increases the maximum normal stress at the clamped end. The increase in the maximum normal stress through the clamped end becomes greater as the ellipticity ratio increases and/or the radius-to-thickness ratio decreases. Besides, it tends to become greater as the ratio of the elasticity moduli of functionally graded material constituents decreases. As the ellipticity decreases, the maximum normal stress at the clamped end decreases.

The Shear Stress: As the radius-to-thickness ratio increases from 5 to 25 for TFG circular beams when the ratio of the elasticity moduli of functionally graded material constituents is 5.43, the shear stress on the axis becomes 23.41 times greater at normalized tangential coordinate 0.05 within the range of St. Venant principle. As the radius-to-thickness ratio decreases, its' influence on the decrease in the maximum shear stress at normalized tangential coordinate 0.05 becomes greater. Similar relation is obtained for the ellipticity ratio except when the radius-to-thickness ratio is 25. As the ratio of the elasticity moduli of functionally graded material constituents increases the maximum shear stress at the clamped end increases. The increase in the shear stress through the clamped end becomes greater as the ellipticity and/or the radius-to-thickness and/or the elasticity moduli ratios increase.

Acknowledgements The author gratefully acknowledges Dr. Mehmet Hakkı Omurtag, Dr. Akif Kutlu and Dr. Emrah Madenci.

Declarations

Conflict of interest The author declares that he has no known competing financial interests or personal relationships that could have appeared to influence the work reported in this paper.

References

1. Thai H-T, Vo TP (2012) Bending and free vibration of functionally graded beams using various higher-order shear deformation beam theories. Int J Mech Sci 62:57–66. https://doi.org/10.1016/j.ijmecsci.2012.05.014
2. Kutlu A (2021) Mixed finite element formulation for bending of laminated beams using the refined zigzag theory. Proc Inst Mech Eng Part J Mater Des Appl 235:1712–1722. https://doi.org/10.1177/14644207211018839
3. Dorduncu M, Kutlu A, Madenci E (2022) Triangular C0 continuous finite elements based on refined zigzag theory 2,2 for free and forced vibration analyses of laminated plates. Compos Struct 281:115058. https://doi.org/10.1016/j.compstruct.2021.115058
4. Madenci E (2021) Free vibration and static analyses of metal-ceramic FG beams via high-order variational MFEM. Steel Compos Struct 39:493–509
5. Calim FF, Cuma YC (2022) Vibration analysis of nonuniform hyperboloidal and barrel helices made of functionally graded material. Mech Based Des Struct Mach 50:3781–3795. https://doi.org/10.1080/15397734.2020.1822181
6. Dorduncu M, Kutlu A, Madenci E, Rabczuk T (2022) Nonlocal modeling of bi-material and modulus graded plates using peridynamic differential operator. Eng Comput. https://doi.org/10.1007/s00366-022-01699-2
7. Dorduncu M, Olmus I, Rabczuk T (2022) A peridynamic approach for modeling of two dimensional functionally graded plates. Compos Struct 279:114743. https://doi.org/10.1016/j.compstruct.2021.114743
8. Sayyad AS, Ghugal YM (2017) Bending, buckling and free vibration of laminated composite and sandwich beams: A critical review of literature. Compos Struct 171:486–504. https://doi.org/10.1016/j.compstruct.2017.03.053
9. Chen Y, Jin G, Zhang C et al (2018) Thermal vibration of FGM beams with general boundary conditions using a higher-order shear deformation theory. Compos Part B Eng 153:376–386. https://doi.org/10.1016/j.compositesb.2018.08.111
10. Karamanlı A (2018) Free vibration analysis of two directional functionally graded beams using a third order shear deformation theory. Compos Struct 189:127–136. https://doi.org/10.1016/j.compstruct.2018.01.060

11. Pei YL, Geng PS, Li LX (2018) A modified higher-order theory for FG beams. Eur J Mech–ASolids 72:186–197. https://doi.org/10.1016/j.euromechsol.2018.05.008
12. Ebrahimi F, Jafari A (2018) A four-variable refined shear-deformation beam theory for thermo-mechanical vibration analysis of temperature-dependent FGM beams with porosities. Mech Adv Mater Struct 25:212–224. https://doi.org/10.1080/15376494.2016.1255820
13. Akbaş ŞD (2018) Forced vibration analysis of functionally graded porous deep beams. Compos Struct 186:293–302. https://doi.org/10.1016/j.compstruct.2017.12.013
14. Ahmadi I, Davarpanah M, Sladek J et al (2023) A size-dependent meshless model for free vibration analysis of 2D-functionally graded multiple nanobeam system. J Braz Soc Mech Sci Eng 46:11. https://doi.org/10.1007/s40430-023-04580-5
15. Ermis M, Kutlu A, Eratlı N, Omurtag MH (2022) Free vibration of axially FG curved beam on orthotropic Pasternak foundation via mixed FEM. J Braz Soc Mech Sci Eng 44:597. https://doi.org/10.1007/s40430-022-03853-9
16. Tang Y, Ma Z-S, Ding Q (2022) On the vibration, buckling and dynamic stability of three-directional functionally graded circular cylindrical tubes with consideration of higher-order beam theory. Int J Appl Mech 14:2250012. https://doi.org/10.1142/S1758825122500120
17. Rajput M, Gupta A (2023) Strain gradient-based thermomechanical nonlinear stability behavior of geometrically imperfect porous functionally graded nanoplates. J Eng Mech 149:04023040. https://doi.org/10.1061/JENMDT.EMENG-6910
18. Lee JK, Choi JM, Kim GS, Lee BK (2024) Generalized flexural rigidity of laterally functionally graded material cross sections and its application to cantilever beam elasticas. J Braz Soc Mech Sci Eng 46:63. https://doi.org/10.1007/s40430-023-04649-1
19. Ebrahimi F, Ghazali M, Dabbagh A (2024) Effect of temporal nonlocality on wave propagation behaviors of viscoelastic FGM nanoshells. J Braz Soc Mech Sci Eng 46:126. https://doi.org/10.1007/s40430-024-04701-8
20. Uzun B, Yayli MÖ (2024) Rotary inertia effect on dynamic analysis of embedded FG porous nanobeams under deformable boundary conditions with the effect of neutral axis. J Braz Soc Mech Sci Eng 46:111. https://doi.org/10.1007/s40430-023-04605-z
21. Null A, Singh SJ, Padhee SS (2024) Analytic solution of Timoshenko-Like deformation in bidirectional functionally graded beams. J Eng Mech 150:04023118. https://doi.org/10.1061/JENMDT.EMENG-7317
22. Li W, Ma H, Gao W (2019) A higher-order shear deformable mixed beam element model for accurate analysis of functionally graded sandwich beams. Compos Struct 221:110830. https://doi.org/10.1016/j.compstruct.2019.04.002
23. Madenci E (2019) A refined functional and mixed formulation to static analyses of fgm beams. Struct Eng Mech Int'l J 69:427–437
24. Safa A, Hadji L, Bourada M, Zouatnia N (2019) Thermal vibration analysis of FGM beams using an efficient shear deformation beam theory. Earthq Struct 17:329–336. https://doi.org/10.12989/eas.2019.17.3.329
25. Lei J, He Y, Li Z et al (2019) Postbuckling analysis of bi-directional functionally graded imperfect beams based on a novel third-order shear deformation theory. Compos Struct 209:811–829. https://doi.org/10.1016/j.compstruct.2018.10.106
26. Montalto EJ, Konstantinidis D (2024) Buckling of short beams considering shear warping: application to fiber-reinforced elastomeric isolators. J Eng Mech 150:04023105. https://doi.org/10.1061/JENMDT.EMENG-7198
27. Bekhadda A, Bensaid I, Cheikh A, Kerboua B (2019) Static buckling and vibration analysis of continuously graded ceramic-metal beams using a refined higher order shear deformation theory. Multidiscip Model Mater Struct 15:1152–1169. https://doi.org/10.1108/MMMS-03-2019-0057
28. Castañeda WM, Yarasca J, Mantari JL (2019) Best shear deformation theories based on polynomial expansions for sandwich beams. Eng Struct 190:422–434. https://doi.org/10.1016/j.engstruct.2019.04.022
29. Zhao F (2023) Real-time shape sensing of composite and sandwich structures by coupling inverse finite-element method with refined zigzag theory. J Eng Mech 149:04023070. https://doi.org/10.1061/JENMDT.EMENG-7093
30. Malikan M, Eremeyev VA (2020) A new hyperbolic-polynomial higher-order elasticity theory for mechanics of thick FGM beams with imperfection in the material composition. Compos Struct 249:112486. https://doi.org/10.1016/j.compstruct.2020.112486
31. Melaibari A, Abo-bakr RM, Mohamed SA, Eltaher MA (2020) Static stability of higher order functionally graded beam under variable axial load. Alex Eng J 59:1661–1675. https://doi.org/10.1016/j.aej.2020.04.012
32. Todorovska MI, Ali H, Rahmani M (2023) Functionally graded beams as surrogate structural models: shear beam with exponentially graded rigidity. J Eng Mech 149:04023027. https://doi.org/10.1061/JENMDT.EMENG-6962
33. Li W, Gao W, Chen S (2020) A material-based higher-order shear beam model for accurate analyses of FG beams with arbitrary material distribution. Compos Struct 245:112253. https://doi.org/10.1016/j.compstruct.2020.112253
34. Pavan GS, Muppidi H, Dixit J (2022) Static, free vibrational and buckling analysis of laminated composite beams using isogeometric collocation method. Eur J Mech - ASolids 96:104758. https://doi.org/10.1016/j.euromechsol.2022.104758
35. Ma H (2020) Rational approach for higher-order shear deformation beam theories. Compos Struct 251:112599. https://doi.org/10.1016/j.compstruct.2020.112599
36. Avcar M, Hadji L, Civalek Ö (2021) Natural frequency analysis of sigmoid functionally graded sandwich beams in the framework of high order shear deformation theory. Compos Struct 276:114564. https://doi.org/10.1016/j.compstruct.2021.114564
37. Tran TT, Nguyen NH, Do TV et al (2021) Bending and thermal buckling of unsymmetric functionally graded sandwich beams in high-temperature environment based on a new third-order shear deformation theory. J Sandw Struct Mater 23:906–930. https://doi.org/10.1177/1099636219849268
38. Ruocco E, Reddy JN (2023) Analytical solutions of Reddy, Timoshenko and Bernoulli beam models: a comparative analysis. Eur J Mech–ASolids 99:104953. https://doi.org/10.1016/j.euromechsol.2023.104953
39. Le CI, Le NAT, Nguyen DK (2021) Free vibration and buckling of bidirectional functionally graded sandwich beams using an enriched third-order shear deformation beam element. Compos Struct 261:113309. https://doi.org/10.1016/j.compstruct.2020.113309
40. Belarbi M-O, Khechai A, Bessaim A et al (2021) Finite element bending analysis of symmetric and non-symmetric functionally graded sandwich beams using a novel parabolic shear deformation theory. Proc Inst Mech Eng Part J Mater Des Appl 235(11):2482–2504. https://doi.org/10.1177/14644207211005096
41. Czekanski A, Zozulya VV (2021) Vibration analysis of nonlocal beams using higher-order theory and comparison with classical models. Mech Adv Mater Struct 28:1293–1309. https://doi.org/10.1080/15376494.2019.1665761
42. Choi S, Kim YY (2021) Higher-order beam bending theory for static, free vibration, and buckling analysis of thin-walled rectangular hollow section beams. Comput Struct 248:106494. https://doi.org/10.1016/j.compstruc.2021.106494

43. Zhang P, Schiavone P, Qing H (2022) Two-phase local/nonlocal mixture models for buckling analysis of higher-order refined shear deformation beams under thermal effect. Mech Adv Mater Struct 29:7605–7622. https://doi.org/10.1080/15376494.2021.2003489
44. Ziou H, Guenfoud M, Hamza G (2021) A simple higher-order shear deformation theory for static bending analysis of functionally graded beams. Jordan J Civ Eng 15:209–224
45. Belarbi M-O, Houari MSA, Hirane H et al (2022) On the finite element analysis of functionally graded sandwich curved beams via a new refined higher order shear deformation theory. Compos Struct 279:114715. https://doi.org/10.1016/j.compstruct.2021.114715
46. Pei YL, Li LX (2021) A simplified theory of FG curved beams. Eur J Mech–ASolids 85:104126. https://doi.org/10.1016/j.euromechsol.2020.104126
47. Sayyad AS, Ghugal YM (2019) A sinusoidal beam theory for functionally graded sandwich curved beams. Compos Struct 226:111246
48. Karami B, Janghorban M, Shahsavari D et al (2019) nonlocal buckling analysis of composite curved beams reinforced with functionally graded carbon nanotubes. Molecules 24:2750. https://doi.org/10.3390/molecules24152750
49. Belarbi M-O, Garg A, Houari M-S-A et al (2022) A three-unknown refined shear beam element model for buckling analysis of functionally graded curved sandwich beams. Eng Comput 38:4273–4300. https://doi.org/10.1007/s00366-021-01452-1
50. Lezgy-Nazargah M, Etemadi E, Hosseinian SR (2022) Assessment of four-variable refined shear deformation theory for low-velocity impact analysis of curved sandwich beams. Eur J Mech–ASolids 94:104604. https://doi.org/10.1016/j.euromechsol.2022.104604
51. Fariborz J, Batra RC (2019) Free vibration of bi-directional functionally graded material circular beams using shear deformation theory employing logarithmic function of radius. Compos Struct 210:217–230. https://doi.org/10.1016/j.compstruct.2018.11.036
52. Javani M, Kiani Y, Eslami MR (2019) Free vibration of arbitrary thick FGM deep arches using unconstrained higher-order shear deformation theory. Thin-Walled Struct 136:258–266. https://doi.org/10.1016/j.tws.2018.12.020
53. Avhad PV, Sayyad AS (2020) Static analysis of functionally graded composite beams curved in elevation using higher order shear and normal deformation theory. Mater Today Proc 21:1195–1199. https://doi.org/10.1016/j.matpr.2020.01.069
54. Sayyad AS, Avhad PV (2022) A new higher order shear and normal deformation theory for the free vibration analysis of sandwich curved beams. Compos Struct 280:114948. https://doi.org/10.1016/j.compstruct.2021.114948
55. Sayyad AS, Avhad PV (2022) Higher-order model for the thermal analysis of laminated composite, sandwich, and functionally graded curved beams. J Therm Stress 45:382–400. https://doi.org/10.1080/01495739.2022.2050476
56. Tran Thi Thu T (2024) Isogeometric analysis for nonlocal vibration characteristics of BFGP curved nanobeams with variable nonlocal parameters. J Eng Mech 150:04024001. https://doi.org/10.1061/JENMDT.EMENG-7219
57. Aribas UN, Atalay M, Omurtag MH (2023) Warping included mixed finite elements for bending and stresses of functionally graded exact curved beams. Mech Adv Mater Struct. https://doi.org/10.1080/15376494.2023.2211075
58. Aribas UN, Aydin M, Atalay M, Omurtag MH (2023) Cross-sectional warping and precision of the first-order shear deformation theory for vibrations of transversely functionally graded curved beams. Appl Math Mech 44:2109–2138. https://doi.org/10.1007/s10483-023-3065-6
59. Aribas UN, Ermis M, Kutlu A et al (2022) Forced vibration analysis of composite-geometrically exact elliptical cone helices via mixed FEM. Mech Adv Mater Struct 29:1456–1474. https://doi.org/10.1080/15376494.2020.1824048
60. Çömez İ, Aribas UN, Kutlu A, Omurtag MH (2022) Two-dimensional solution of functionally graded piezoelectric-layered beams. J Braz Soc Mech Sci Eng 44:101. https://doi.org/10.1007/s40430-022-03414-0
61. Aribas UN, Ermis M, Omurtag MH (2021) The static and stress analyses of axially functionally graded exact super-elliptical beams via mixed FEM. Arch Appl Mech 91:4783–4796. https://doi.org/10.1007/s00419-021-02033-w
62. Aribas UN, Ermis M, Eratli N, Omurtag MH (2019) The static and dynamic analyses of warping included composite exact conical helix by mixed FEM. Compos Part B Eng 160:285–297. https://doi.org/10.1016/j.compositesb.2018.10.018
63. Aribas UN, Ermis M, Kutlu A et al (2018) Forced vibration analysis of warping considered curved composite beams resting on viscoelastic foundation. Gazi Univ J Sci 31:1093–1105
64. Ermis M, Omurtag MH (2017) Static and dynamic analysis of conical helices based on exact geometry via mixed FEM. Int J Mech Sci 131–132:296–304. https://doi.org/10.1016/j.ijmecsci.2017.07.010
65. Wakashima K, Hirano T, Niino M (1990) Space applications of advanced structural materials. ESA SP 303:97
66. Reddy JN (1984) A simple higher-order theory for laminated composite plates. J Appl Mech 51:745–752. https://doi.org/10.1115/1.3167719
67. Touratier M (1991) An efficient standard plate theory. Int J Eng Sci 29:901–916. https://doi.org/10.1016/0020-7225(91)90165-Y
68. Soldatos KP (1992) A transverse shear deformation theory for homogeneous monoclinic plates. Acta Mech 94:195–220. https://doi.org/10.1007/BF01176650
69. Aydogdu M (2009) A new shear deformation theory for laminated composite plates. Compos Struct 89:94–101. https://doi.org/10.1016/j.compstruct.2008.07.008
70. Bhimaraddi A, Chandrashekhara K (1993) Observations on higher-order beam theory. J Aerosp Eng 6:408–413. https://doi.org/10.1061/(ASCE)0893-1321(1993)6:4(408)
71. Jones RM (1999) Mechanics of composite materials, 2nd edn. Taylor & Francis, Philadelphia
72. Doğruoğlu AN, Omurtag MH (2000) Stability analysis of composite-plate foundation interaction by mixed fem. J Eng Mech 126:928–936. https://doi.org/10.1061/(ASCE)0733-9399(2000)126:9(928)
73. Omurtag MH, Aköz AY (1994) Hyperbolic paraboloid shell analysis via mixed finite element formulation. Int J Numer Methods Eng 37:3037–3056. https://doi.org/10.1002/nme.1620371803
74. Ermis M, Kutlu A, Eratlı N, Omurtag MH (2018) The dynamic analysis of a linear viscoelastic planar elliptical beam. Sigma J Eng Nat Sci 9:157–168

Authors and Affiliations

Umit N. Aribas[1]

✉ Umit N. Aribas
umit.aribas@medipol.edu.tr

[1] Department of Civil Engineering, School of Engineering and Natural Sciences, Istanbul Medipol University, 34810 Istanbul, Türkiye